ELSEVIER

Contents lists available at ScienceDirect

Marine Chemistry

journal homepage: www.elsevier.com/locate/marchem





Differential manganese and iron recycling and transport in continental margin sediments of the Northern Gulf of Mexico

Shannon M. Owings ^a, Laurie Bréthous ^b, Eryn M. Eitel ^a, Benjamin P. Fields ^a, Anthony Boever ^a, Jordon S. Beckler ^c, Bruno Bombled ^b, Bruno Lansard ^b, Edouard Metzger ^d, Christophe Rabouille ^b, Martial Taillefert ^a, ^{*}

- ^a School of Earth and Atmospheric Sciences, Georgia Institute of Technology, Atlanta, GA 30332, United States of America
- b Laboratoire des Sciences du Climat et de l'Environnement (LSCE), UMR 8212, IPSL-CEA-CNRS-UVSQ-Université Paris Saclay, 91198 Gif-sur-Yvette, France
- ^c Florida Atlantic University, Harbor Branch Oceanographic Institute, Boca Raton, FL 33431, United States of America
- d UMR CNRS 6112 LPG-BIAF, Université d'Angers, 49045 Angers Cedex, France

ARTICLE INFO

Keywords: Diagenetic processes Manganese and iron cycling Sulfate Reduction Continental slope sediments River-dominated margins Mississippi delta Northern Gulf of Mexico

ABSTRACT

Pore water and solid phase geochemical profiles of sediment cores collected along two transects on the western and eastern sides of the Mississippi River mouth in the northern Gulf of Mexico were incorporated into a reactive transport model to determine the role of manganese and iron in the remineralization of carbon. Reactive transport model calculations indicate that sedimentation rates control the intensity of anaerobic carbon remineralization and select for the dominant anaerobic carbon remineralization pathways. Although sulfate reduction dominates the shelf station (65 m water depth), denitrification and microbial manganese reduction appear equally significant anaerobic respiration processes along the continental slope the closest to the Mississippi River, whereas microbial iron reduction does not represent an important process in these sediments. These findings suggest that the differential kinetics of manganese and iron redox transformations influence carbon remineralization processes on the continental slope. The fast kinetics of Fe²⁺ oxidation near the sediment-water interface and high sedimentation rates maintain Fe under the form of Fe(III) oxides and thermodynamically prevent sulfate reduction from dominating carbon remineralization processes on the slope, whereas the much slower Mn²⁺ oxygenation kinetics allows diffusion of Mn²⁺ across the sediment-water interface of the shelf station closest to the river mouth. Exposure to oxygenated bottom waters and entrainment within mobile muds typical of deltaic sediments during high riverine discharge likely promote the formation and downslope transport of Mn (III/IV) oxides within the nepheloid layer. This phenomenon appears to form a manganese 'conveyor belt' that selectively enriches Mn(III/IV) oxides relative to Fe(III) oxides in the deep sediment. In contrast, the intensity of anaerobic carbon remineralization processes along the eastern continental slope the farthest from the Mississippi River plume is much lower due to the low organic and lithogenic inputs, and denitrification dominates anaerobic respiration. Overall, these findings suggest that manganese cycling and its role in carbon remineralization processes in continental slope sediments exposed to large riverine inputs may be more important than previously considered.

1. Introduction

Riverine-dominated continental margins (RiOMars) represent carbon remineralization hot spots as a result of the significant input of natural organic matter and inorganic particulate material from terrestrial origin (Bianchi et al., 2018). In addition, the nutrient supply from the underlying sediment (Aller et al., 1996; Grégoire and Friedrich,

2004; Morse and Rowe, 1999) or riverine inputs (Turner et al., 2007) promotes primary production on continental shelves that may enhance the overall input of natural organic matter to the seafloor (Aller et al., 1996; Waterson and Canuel, 2008) and increase diagenetic reactivity by a priming effect (Bianchi, 2011). The supply of organic matter and lithogenic material to continental shelves depends on the intensity of riverine discharge, which typically varies seasonally (Bianchi et al.,

E-mail address: mtaillef@eas.gatech.edu (M. Taillefert).

^{*} Corresponding author.

2007; Mossa, 1996). At low river discharge, the density difference between freshwater and seawater impedes the seaward transport of freshwater and its particulate load such that freshwater and sediment are both trapped in the estuary or backwater reaches of rivers (Allison et al., 2012; Geyer et al., 2004). In contrast, the momentum of the river outflow at high discharge is strong enough to overcome this effect and transport water and sediment offshore. As a result, sediment trapped in estuaries or backwater reaches during low discharge seasons is biogeochemically processed until the next high discharge, such that the inorganic (Allison and Pratt, 2017; Meiggs and Taillefert, 2011; Sutula et al., 2004) and organic (Cowie and Hedges, 1984; Cowie and Hedges, 1992; Sampere et al., 2011) content of surrounding shelf sediments is affected seasonally. In turn, the lithologic input to continental shelves is greater during high discharge as a result of increased erosion upstream (Meiggs and Taillefert, 2011). Riverine dissolved and particulate material eventually delivered to the ocean flocculates and aggregates into fine-grained material that settles into the benthic boundary layer (BBL) 0.1-2 m above the seabed and forms mobile muds, an ephemeral layer that is often remobilized by physical mixing generated by tidal currents or storms (Aller, 1982; Aller, 1998; McKee et al., 2004). These mobile muds are eventually deposited on continental shelves and slopes, with selective dispersal that depends on particle size, density, morphology, or composition (McKee et al., 2004), and enhance carbon remineralization by exposing sediment to oxygenated bottom waters (Aller, 1998; Blair and Aller, 2012; Hartnett et al., 1998) and co-metabolizing fresh, planktonic organic carbon (Canfield, 1994). As a result, sediment distribution across continental margins and their associated diagenetic processes may vary widely depending on the organic carbon and lithologic composition of the top sediment layers (Canfield, 1994; Grégoire and Friedrich, 2004; Taillefert et al., 2017).

The complex interplay between abiotic and biotic processes influences the availability of electron acceptors and efficiency of carbon remineralization processes. After aerobic respiration, sulfate reduction often plays a large role in marine sediments exposed to significant inputs of natural organic matter (Bowles et al., 2014; Ferdelman et al., 1999; Jørgensen, 1982; Lee et al., 2008; Lin et al., 2002) mainly due to the high concentration of sulfate in seawater and the efficient carbon remineralization yield of this process (i.e., 2 mol of carbon per mole of sulfate reduced). In RiOMars and shelf to slope transition zones of passive continental margins, however, manganese (Mn) and iron (Fe) reduction may contribute to a large fraction of carbon remineralization processes (Aller et al., 1990; Beckler et al., 2016; Canfield et al., 1993a; Canfield et al., 1993b; Devereux et al., 2015; Hyun et al., 2017; Law et al., 2009; Oldham et al., 2019; Sørensen and Jeørgensen, 1987; Thamdrup et al., 2000). The differential kinetics of Mn and Fe transformations also separates Mn^{2+} and Fe^{2+} vertically in the sediment column. Indeed, microbial Mn(III/IV) oxide reduction is thermodynamically more favorable and much faster than microbial Fe(III) reduction (Arnold et al., 1988; Dollhopf et al., 2000; Larsen et al., 1998; Lovley and Phillips, 1988; Myers and Nealson, 1988) whereas abiotic Fe²⁺ oxidation is much faster than abiotic (Stumm and Morgan, 1996) and biologically mediated Mn^{2+} oxidation even if abiotic and biotic Mn^{2+} oxidation rates in natural environments are difficult to disentangle (Richard et al., 2013). As a result, Mn²⁺ diffuses out of the sediment and is slowly reoxidized either close to the sediment surface (Mouret et al., 2009) or in the overlying waters (Trefry and Presley, 1982), whereas Fe²⁺ is oxidized immediately at the oxic-anoxic transition (Millero et al., 1987) and may either precipitate as Fe(III) oxides or remain soluble under the form of organic-Fe(III) complexes in the presence of natural organic ligands (Taillefert et al., 2000; Beckler et al., 2015). These processes and the oxidation of reduced sulfur minerals are promoted by bioturbation and bioirrigation which enhance the oxygen supply to the first tens of centimeters of sediment (Aller, 1994; Canfield et al., 1993b). Simultaneously, Fe^{2+} is less mobile in comparison to Mn^{2+} due to rapid precipitation with H₂S (Pyzik and Sommer, 1981). Mn(III, IV) oxides are therefore dispersed and redeposited in surface sediments where they

become important electron acceptors for organic carbon oxidation (Hyun et al., 2017; Law et al., 2009), whereas Fe(III) oxides are typically immobilized below the oxygen penetration depth in the sediment where they can eventually be utilized for organic matter degradation, with possible production of organic-Fe(III) complexes as soluble intermediates (Taillefert et al., 2007; Jones et al., 2010). Differentiating these processes in RiOMar sediments may help quantify anaerobic carbon remineralization processes more accurately.

This study investigated the main redox processes involved in the transformation of natural organic matter in continental shelf and slope sediments of the northern Gulf of Mexico (nGoM). Two cross slope transects were studied to examine the effect of lithogenic and organic carbon inputs on diagenetic processes. The first transect is influenced by inputs from the Mississippi River and the other, to the east of the Mississippi River plume, is not exposed to significant inputs. At each station, depth profiles with potentiometric, amperometric, and voltammetric microelectrodes in intact sediment cores were combined with conventional pore water analyses and solid phase chemical extractions of the same sediment cores. Finally, a one-dimensional transient reactive transport model run to steady-state was also used to estimate carbon remineralization rates and identify the role of lithogenic inputs on microbial metal reduction.

2. Methods

2.1. Field site and sediment sampling

The continental margin of the nGoM is well known for its seasonal hypoxic zone (defined as $<63 \,\mu\text{M} \, \text{O}_{2(aq)}$) resulting from the high input of freshwater and nutrients from fertilizers from the Mississippi-Atchafalaya River System (MARS) (Rabalais et al., 2007). The limited circulation and strong water column stratification based on the differences in density of fresh and marine waters, together with nutrientstimulated local production promote the depletion of dissolved oxygen in the deep waters (Fennel and Testa, 2019). In addition, the continental margin of the nGoM is a unique region to study the effect of riverine inputs on diagenetic processes in RiOMar sediments as the continental margin receives approximately 2.1×10^8 tons of sediment per year (Milliman and Meade, 1983) and an annual mass load of 7.38×10^7 tons of metals (Reiman et al., 2018) from the MARS under the form of a particulate plume that covers as much as $2400 \pm 400 \text{ km}^2$ in the summer (Green et al., 2006; Xu et al., 2014). The transport of material extends beyond the hypoxic region and can be transferred to the nearby Mississippi canyon (Bianchi et al., 2006) via lateral down-slope accretion of material from the margins and/or mass wasting (Rowe et al., 2008).

Sediment cores (9.6 cm inner diameter x 70 cm) were collected using a multi-corer (MC 800, Ocean Instruments) onboard the R/V Savannah along the Louisiana shelf and slope during an oceanographic cruise from July 25 to August 6, 2017 (Fig. 1 and Table 1). Station locations were selected along a transect near the outlet of the Mississippi River across the slope and toward the Mississippi canyon stations referred to as the 'western transect' with respect to positioning of the Mississippi River: St. 2b (65 m), St. 13 (510 m), and St. 11 (925 m) (Table 1 and Fig. 1). Two additional stations were selected to the east of the Mississippi River along a transect across the continental slope which is referred to as the 'eastern transect': St. 15 (274 m) and St. 12 (989 m) (Table 1 and Fig. 1). Stations were named based on the labelling of stations from previous expeditions (Beckler et al., 2016).

2.2. O2 and pH microprofiles and porosity profiles

Bottom water samples were collected as close to the seafloor as possible (i.e. 2 m) using the rosette of 12 L Niskin bottles (OceanTest Equipment, Inc). Bottom water pH was measured using the m-cresol purple spectrophotometric method (Clayton and Byrne, 1993; Dickson et al., 2007; Rassmann et al., 2016) and recalculated at in situ

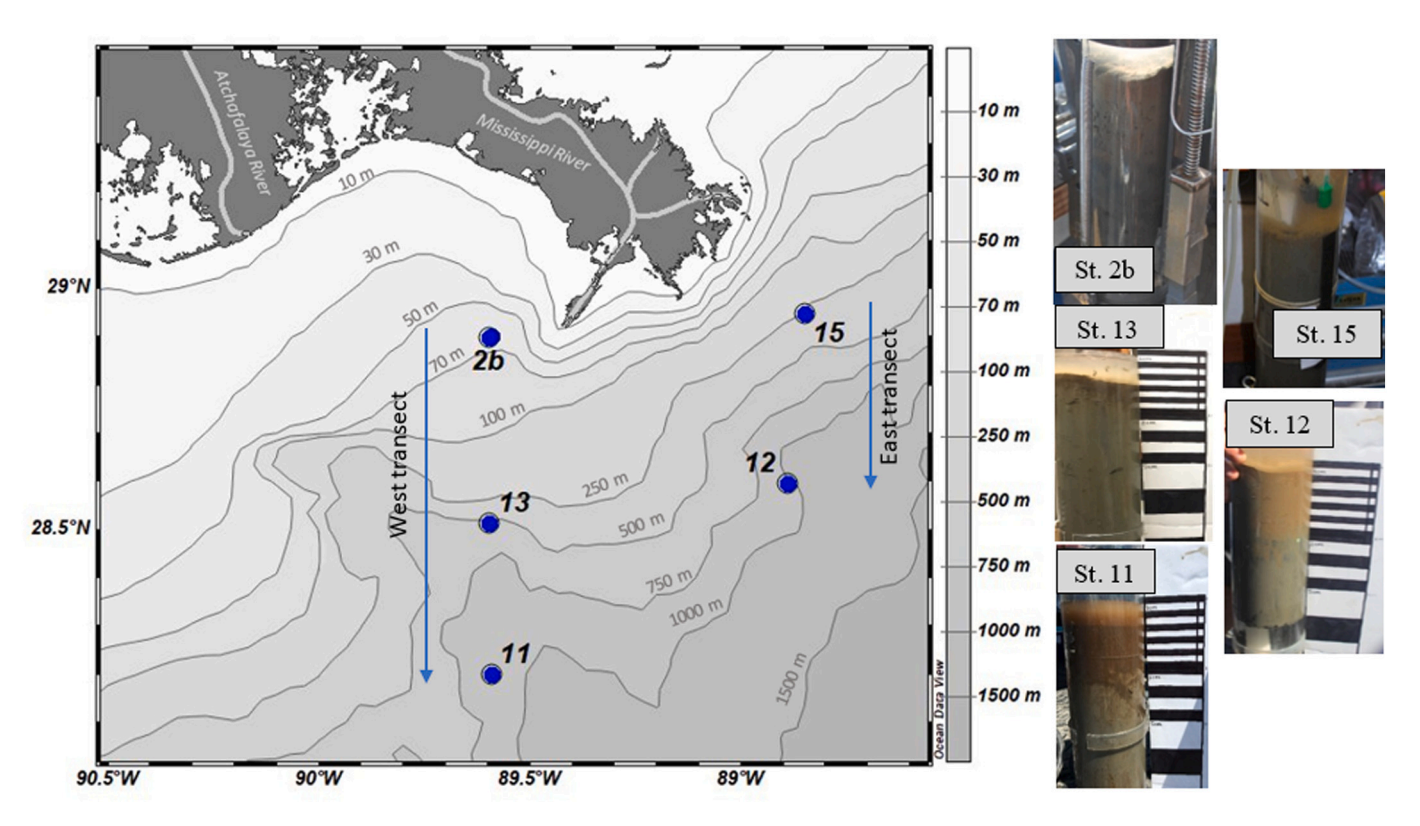


Fig. 1. a) Map of the stations across the Louisiana shelf and slope in the northern Gulf of Mexico where benthic landers were deployed and sediment cores collected during a research cruise in July and August of 2017. The two transects, east and west, are labeled with arrows. Depth contours (m) indicate ocean bathymetry; b) pictures of the cores showing contrasting sediment colors at the different sampling locations and color variations with depth in each core. Thin, medium, and thick white and black lines represent depth intervals of 1, 2 and 5 cm respectively.

Table 1
Station location, water column depth, and corresponding bottom water parameters (temperature, salinity, oxygen concentration, pH) along the western (St.2b, 13, 11) and eastern (St. 15 and 12) transects.

Station	Latitude (N)	Longitude (W)	Depth (m)	Temp (°C)	Salinity	O ₂ [μM] (% sat)	pН
St. 2b	28°54.033	89°35.417	65	22.5	36.3	114.7 (48%)	7.86
St. 13	28°30.721	89°35.730	510	9.4	34.9	126.4 (44%)	7.80
St. 11	28°12.043	89°35.486	925	11.5	33.4	130.0 (47%)	7.78
St. 15	28°56.855	88°50.903	274	13.2	35.4	122.5 (47%)	7.86
St. 12	28°35.896	88°53.435	989	13.9	34.7	186.3 (72%)	7.76

O2% sat calculated relative to saturated O2 estimated from in situ temperature and salinity

temperature using salinity and total alkalinity (TA). Bottom water O_2 concentrations were determined by Winkler titration (Grasshoff et al., 1999) and oxygen saturation levels related to maximum oxygen concentrations (100% saturation) determined at the measured temperature and salinity with USGS DO tables (https://water.usgs.gov/software/DOTABLES/).

In situ oxygen and pH profiles were collected at St. 2b in 100 μ m increments using an autonomous benthic lander with a high-resolution micromanipulator (Unisense®) equipped with a resistivity probe (Revsbech, 1989) and O₂ (Andrews and Bennett, 1981) and pH microsensors. For all other stations, ex situ O₂ and pH microprofiles were obtained with a 200 μ m resolution in the same core using the same microsensors deployed on a laboratory micromanipulator (Unisense®). During ex situ profiling, overlying water temperature, oxygen concentrations, and pH were monitored and maintained at bottom water conditions by bubbling a mixture of air, N₂, and CO₂ using a 3-way valve and circulating the overlying water through a thermostatic bath. The pH probes were practically calibrated with NBS buffers at pH 4, 7, and 10, but the pH profiles were adjusted using the spectrophotometrically measured bottom water pH at the in situ temperature (Rassmann et al., 2016). All pH values are reported on the total proton scale (pH_T).

Oxygen sensors were calibrated using oxygen concentrations determined in bottom waters and their responses in the anoxic zone (Cai and Sayles, 1996). Two pH and two oxygen profiles were obtained successively in most of the sediment cores within 2–3 h. After completion of the pH and $\rm O_2$ microprofiles, the same core was sectioned in 3–60 mm sections with higher resolution at the surface of the core. Sediment samples were frozen (–20 $^{\circ}\rm C)$ and porosity was determined back at the LSCE by measuring the difference between wet and dry sediment weight after heating at 60 $^{\circ}\rm C$ for 10 days and using a sediment density of 2.65 g cm $^{-3}$.

2.3. Voltammetric ex situ profiling

A replicate core collected from the same MC800 deployment was profiled in millimeter increments with 100 μm gold/mercury (Au/Hg) voltammetric microelectrodes deployed on a computer-controlled micromanipulator with DLK 70 or 100 potentiostat (Analytical Instrument Systems, Inc.) in a three-electrode system (Ag/AgCl reference, Pt counter, and Au/Hg working electrodes). Au/Hg microelectrodes were fabricated as previously reported (Luther et al., 2008) and prepared daily by electrodeposition of mercury (Brendel and Luther III, 1995).

Dissolved oxygen was measured using linear sweep scans from -0.1 to -1.8 V and a scan rate of 200 mV s⁻¹ after a conditioning step at -0.1 Vfor 10 s (Minimum Detection Limit: MDL $\sim 5 \,\mu M$) (Luther et al., 2008). At each depth, cathodic square wave scans with a preconditioning step at -0.1 V for 10 s were run in at least triplicate from -0.1 to -1.8 V with a scan rate of 200 mV s⁻¹. These scans are used to quantify dissolved manganese(II) (Mn²⁺, MDL \sim 15 μ M), dissolved iron(II) (Fe²⁺, MDL \sim 25 μ M), thiosulfate (S₂O₃²⁻, MDL \sim 10 μ M), and total dissolved sulfide $(\Sigma H_2 S = H_2 S + H S^- + S^0 + S_x^{2-}, MDL \sim 0.2 \ \mu M)$ in addition to qualitatively detect organic complexes of Fe(III) (org-Fe(III)) (Taillefert et al., 2000) and aqueous iron sulfide clusters (FeS_(aq)) (Theberge and Luther, 1997). When ΣH_2S or org-Fe(III) species were present, an additional preconditioning step was applied at -0.9 V for 10 s before each scan to avoid memory effects. Voltammetric signals were integrated using a semi-automated VOLTINT software package (Bristow and Taillefert, 2008). Before profiling, working electrodes were calibrated in a cell stand with MnCl₂ (0–400 μ M Mn²⁺), and Fe²⁺, Σ H₂S, and S₂O₃²⁻ were quantified from the pilot ion method with Mn²⁺ as pilot ion (Brendel and Luther III, 1995). Oxygen concentrations in the overlying waters were calibrated using the bottom water oxygen concentrations determined by Winkler titration. As the chemical composition of org-Fe(III) complexes and FeS(aq) is unknown, these species cannot be quantified (Taillefert et al., 2000; Theberge and Luther, 1997) and are reported in normalized current intensities (Meiggs and Taillefert, 2011).

2.4. Pore water extraction and analyses

After voltammetric profiles were completed, the same core was immediately transferred to a glove bag (Sigma Aldrich) with a $\rm N_2$ atmosphere for sectioning in 7–10, 20, 50, and 100 mm increment depending on core depth. Sediment sections were partitioned into 50 mL falcon tubes, centrifuged for 10 min at 3000 rpm under $\rm N_2$ atmosphere to extract pore waters, and the leftover sediment sections were frozen at $-20~^{\circ}\rm C$. Extracted pore waters were then filtered through 0.2- μm Whatman® nitrocellulose Puradisc syringe filters into 15 mL falcon tubes under $\rm N_2$ atmosphere and immediately split for onboard analyses (dissolved iron and manganese speciation, dissolved orthophosphate, dissolved inorganic carbon, and total alkalinity). The leftover pore water was preserved at -20 $^{\circ}\rm C$ until analysis at Georgia Tech (dissolved ammonium, chloride, bromide, sulfate, nitrate, nitrite).

Total alkalinity (TA) measurements were conducted according to Dickson et al., 2007, but with a 3 mL open-cell potentiometric titration (Rassmann et al., 2016) using 0.01 M HCl, which was calibrated every day using Dickson standard batch #150 (Rassmann et al., 2016). Error in this analysis represents the standard deviation from the mean of duplicate samples if available or propagation of analytical error for single samples (1%). Dissolved inorganic carbon (DIC) was determined by flow injection analysis, if necessary after 5 mM ZnCl2 amendment to avoid dissolved sulfide interference (Hall and Aller, 1992). Dissolved Mn(III) (Mn³⁺) and total dissolved Mn (Mn_d) were determined in duplicate using the porphyrin kinetic spectrophotometric method (Madison et al., 2011) modified to account for dissolved Fe²⁺ interferences using external calibrations with Fe²⁺-spiked Mn²⁺ standards and independent pore water \mbox{Fe}^{2+} measurements. \mbox{Mn}_d was quantified by converting the final absorbance to concentration using the molar absorptivity ($\epsilon = 91.2$ $\pm~0.4\times10^{-3}~\mu M~cm^{-1})$ determined from external calibration curves with Mn²⁺ (MDL: 0.11 μ M, 3 σ of blanks, n = 24). Mn³⁺ was quantified by fitting the spectrophotometric kinetic curve as an exponential rise to a maximum curve but was below detection limit (MDL $< 1.5 \, \mu M$) in the majority of pore water samples. Dissolved orthophosphates (ΣPO_4^{3-}) were quantified with the methylene blue method after correction for silica interference (Murphy and Riley, 1962). Finally, dissolved Fe²⁺ was quantified using the ferrozine method without hydroxylamine while total dissolved Fe (Fe_d) was determined by reacting a separate aliquot with hydroxylamine hydrochloride (0.2 M) in the dark for 24 h. Dissolved Fe(III) (Fe(III)_d) was obtained by subtracting the dissolved Fe²⁺

concentration from total dissolved Fe (Stookey, 1970; Viollier et al., 2000). At Georgia Tech, NH $_{\rm T}^{+}$ was quantified by the indophenol blue method (Strickland and Parsons, 1972) and anions via HPLC with UV detection using a 3.2 mM NaCO $_3$ / 1.0 mM NaHCO $_3$ buffer (SO $_4^{2-}$, Cl $^{-}$, Br $^{-}$; MDL: 218, 422, 114 μ M respectively) and 54 mM NaCl (NO $_2^{-}$ NO $_3^{-}$, MDL = 0.12 and 0.11 μ M) eluents (Beckler et al., 2014). All standard deviations reported for pore water measurements represent analytical error propagated from calibration curves except for SO $_4^{2-}$ at St. 13, St. 11, and St. 12 which represent the standard deviations from duplicate measurements.

2.5. Solid phase analysis

Solid phase manganese and iron were extracted in duplicate from sediments following classical sequential and parallel extraction protocols (Anschutz et al., 2000; Hyacinthe et al., 2001; Hyacinthe and Van Cappellen, 2004; Kostka and Luther, 1994; Tessier et al., 1979). A 0.2-0.5 g pellet of wet sediment was added to a 15 mL falcon tube, and the adsorbed fraction (absorbed Fe²⁺, absorbed Mn²⁺) was first extracted for 2 h on a rotary wheel using 8 mL MgCl₂ (0.5 M, pH 7) (Tessier et al., 1979). The supernatant was removed for analysis and replaced by a 8 mL sodium acetate solution (0.5 M adjusted to pH 5 with acetic acid) to extract Fe²⁺ and Mn²⁺ bound in the carbonate phases (carbonate-bound Fe²⁺, carbonate-bound Mn²⁺) on a rotary wheel for 5 h (Tessier et al., 1979). Finally, the supernatant was replaced by 8 mL of an ascorbate solution (pH 7.4) consisting of sodium citrate (0.2 M), sodium bicarbonate (0.6 M), and 0.1 M L-ascorbic acid for the extraction of poorly crystalline Fe(III) and Mn(III/IV) phases on the rotary wheel for 24 h (Hyacinthe et al., 2001; Kostka and Luther, 1994). The ascorbate fraction reductively dissolves poorly crystalline Fe(III) oxides (i.e., ferrihydrite, Kostka and Luther, 1994; Raiswell et al., 2010) and reactive Mn(III/IV) oxides (Anschutz et al., 2005) but not crystalline iron oxides (e.g., hematite, goethite, magnetite) or FeS_(s) (Kostka and Luther, 1994). In parallel, total reactive Fe (i.e., siderite, poorly crystalline Fe(III), crystalline Fe(III) oxides, and FeS(s)) was extracted in duplicate sediment pellets with a dithionite reagent (0.35 M ammonium acetate, 0.2 M sodium citrate, 0.03 M sodium dithionite, pH 5) at 60 $^{\circ}\text{C}$ in a water bath for 4 h (Kostka and Luther, 1994). The carbonate and ascorbate concentrations were subtracted from the dithionite fraction to quantify crystalline $Fe(III) + FeS_{(s)}$. Between each extraction step, the sediment slurry was centrifuged for 10 min at 3000 rpm and the supernatant was stored in a separate falcon tube at 4 °C until analysis. The supernatant was measured for total extracted Fe²⁺ using the ferrozine method (Stookey, 1970), whereas samples for total dissolved manganese (Mn_d) from the extractions were stored at 4 °C until analysis by Inductively Coupled Plasma – Mass Spectrophotometer (ICP-MS) using appropriate analytical procedures (Owings et al., 2019). In addition, two sediment samples were dried at 50 °C for 3-5 days, allowed to cool in the oven, and weighed to normalize concentrations to the weight of dry sediment in grams (gdw). All errors reported represent the standard deviation of the average of duplicate extractions. Finally, the acid volatile sulfides (AVS) fraction was extracted in triplicate by cold distillation of wet sediment (0.5-0.7 g) with 5 mL of 3 M HCl and entrainment of the H₂S gas product by a pre-purified (using a Cu trap heated at 400 °C to remove O2 traces) ultra-high purity (UHP) N2 stream into a 1 M NaOH solution trap at low flow rate (Henneke et al., 1991). Total dissolved sulfide trapped after 4 h was quantified by absorbance at 230 nm using NaS₂ standards dissolved daily in degassed 1 M NaOH (Ellis and Golding, 1959).

2.6. Calculations

2.6.1. Flux calculations

Dissolved oxygen uptake (DOU) rates and the diffusive fluxes of DIC, NH $_{+}^{+}$, and Σ PO $_{+}^{3-}$, were calculated from their concentration gradients across the sediment-water interface (SWI) using Fick's first law (Eq. (1)),

assuming diffusion mainly controlled transport.

$$F_{i} = -\varphi D_{s} \frac{dC_{i}}{dz} \tag{1}$$

In these calculations, φ represents the average porosity of the sediment layers where the diffusive flux was determined, D_s is the apparent diffusion coefficient after correcting for tortuosity, and $\frac{dC_i}{dx}$ is the concentration gradient of species i as a function of depth z. For all species $D_s = \frac{D_0}{a^2}$, where D_0 is the molecular diffusion coefficient and tortuosity θ^2 = 1 - $\ln(\varphi^2)$. For dissolved oxygen, $D_0 = 4.79 \ 10^{-9} \ \frac{T}{uV^{0.6}}$, where T is the temperature, μ the dynamic viscosity, and V_b the molar volume, whereas for ions $D_0 = (m_0 + m_1 T) 10^{-6} cm^2 s^{-1}$, where m_0 and m_1 are empirically derived constants (Boudreau, 1997). The diffusion coefficients for HCO₃ and HPO₄² were used for the calculations of the diffusive fluxes of DIC and ΣPO_4^{3-} as these species constituted the majority of the carbonate and phosphate speciation in representative solutions for each station modeled using Visual MINTEO version 3.1 (Gustafsson, 2019). Positive fluxes in these calculations represent downward fluxes into the sediment, whereas negative fluxes represent upward fluxes across the SWI. Data from O2 microsensors (Unisense®) were used for DOU rate calculations given their high spatial resolution in the top 20 mm of sediment.

2.6.2. Diagenetic modeling

The MatlabTM-based one-dimensional transient reactive transport model MATSEDLAB (Couture et al., 2010) was used to quantify the depth-integrated rates of aerobic and anaerobic respiration at each of the station investigated. In this model, the transport parameters reflect conventional bioturbation, irrigation, sedimentation, compaction, and diffusion in sediments (Boudreau, 1997; Wang and Van Cappellen, 1996). Porosity was assumed constant at the mean porosity determined in each core (Fig. S1), sedimentation rates were fixed at each station with values from the literature (Corbett et al., 2006; Yeager et al., 2004). Diffusion was assumed molecular and modified to account for salinity, temperature, and tortuosity (Boudreau, 1997). Finally, bioirrigation and bioturbation were considered in the model and assumed to decrease exponentially with depth in the sediment as in previous modeling efforts (Soetaert et al., 1996; Wang and Van Cappellen, 1996; Boudreau, 1997). The bioirrigation coefficient at the sediment-water interface was the same for all species and the decrease in bioirrigation with depth was fitted using the ammonium profiles (Wang and Van Cappellen, 1996). The bioturbation coefficient at the sediment-water interface was predicted from an empirical relationship as a function of water depth (Boudreau, 1997), and the maximum bioturbation depth was set empirically at each station according to the Fe(OH)3 profile. Organic carbon degradation that produces NH₄ and DIC as by-product is described by Michaelis-Menten rate laws with respiratory inhibition (Soetaert et al., 1996; Wang and Van Cappellen, 1996) using C:N ratios from the literature (Sampere et al., 2011; Waterson and Canuel, 2008). Reduced compounds produced during remineralization (i.e., NH₄⁺, Mn^{2+} , Fe^{2+} , $\mathrm{\Sigma H}_2\mathrm{S}$) are partly removed from the system by precipitation of sulfide (FeS) or carbonate minerals (MnCO3, FeCO3) and oxidation in the presence of O_{2(aq)} or other oxidants (MnO₂, Fe(OH)₃) using explicit kinetic formulations (Wang and Van Cappellen, 1996). The whole suite of reactions and rate laws included in the model are provided in the appendix (Tables S1-S4). Boundary conditions included Dirichlet conditions at the sediment surface, using either bottom water concentrations of each dissolved constituent or optimized concentrations of particulate material (i.e. organic carbon, Mn(III/IV) oxides, or Fe(III) oxides), and zero flux (Neumann) conditions at the bottom of the domain. As kinetic parameters and rate laws of most abiotic processes are relatively well characterized, they were fixed in the model (Table S5). In turn, microbial respiration rate constants (Table S6) and other important parameters (Table S7) were optimized to fit depth profiles of the main redox species measured in a self-consistent manner at each station. Data from O₂ microsensors (Unisense®), voltammetric

microelectrodes (ΣH_2S), pore water extractions (DIC, NH₄⁺, NO₃⁻, Mn²⁺, Fe²⁺, and SO₄²⁻), and solid phase extractions (poorly crystalline Fe(III) oxides and Mn(III/IV) oxides, carbonate-bound Fe²⁺, carbonate-bound Mn²⁺, and AVS) were used in these calculations.

3. Results

The stations investigated in this study (Table 1) include St. 2b located in the zone of highest sediment accumulation rate (>2.5 cm yr⁻¹, (Corbett et al., 2006)), while the other stations display relatively low sedimentation rates (<0.1 cm yr⁻¹, (Corbett et al., 2006; Yeager et al., 2004). Percentage of organic carbon content varies between 1.0 and 1.5%, with the highest percentages found at the shallowest stations of each transect (St. 2b, St. 15) (Table 2). The sediment texture and color reflected the different geochemical conditions at each station. St. 2b consisted mainly of dark gray/black mud (Fig. 1) with a band of black sediment below 45 cm (not pictured). St. 13 and St. 11 cores contained light gray muds with flocculant rust and brown colored sediments present in the top 5 and 10 cm, respectively (Fig. 1). The sediments at St. 12 displayed a light orange/brown color in the top 10 cm that transitioned rapidly to gray sediments with black patches after 10 cm (Fig. 1). St. 15 was made of gray mud with rust colored patches.

3.1. Bottom water parameters and oxygen, pH, and porosity microprofiles

Bottom waters, though oxic (Table 1) and outside the hypoxic zone for that season (Rabalais and Turner, 2017), were significantly undersaturated (44–72%) along the continental slope. Dissolved oxygen concentrations decreased exponentially from the SWI to below detection limit at depth. The oxygen penetration depth (OPD) increased across the shelf to slope transects from 1.6 mm at St. 2b to 8.3 and 14.0 mm at St. 13 and 11 along the western transect, and to 7.4 and 9.0 mm at St. 15 and 12 along the eastern transect (Table 2). At St. 15, a pocket of oxygen was detected below the OPD (Fig. 2) likely due to bioirrigation. Bottom water pH $_{\rm T}$ collected from overlying waters of the core varied between 7.76 and 7.86 (Table 1), reflecting the widespread acidification of sediment overlying waters in this environment (Cai et al., 2011). The pH microprofiles collected over the first 5–8 cm at St. 13, 11, 15, and 12

Table 2Sedimentation rate and Organic Carbon (OC) content obtained from the literature and average porosity, oxygen penetration depth (OPD), and diffusive oxygen uptake rate (DOU) determined along the western (St. 2b, 13, 11) and eastern (St. 15 and 12) transectsⁱ.

Station	Sed rate (cm/ year)	OC (%)	Average porosity ^g	OPD (mm) ^h	DOU (mmol/ m ² /d)
St. 2b	>2.5 ^a	1.5 ^d	0.85 ± 0.04	1.6	13.8
St. 13	$< 0.7^{b}$	1.1^{d}	0.87 ± 0.04	8.3	3.6
St. 11	0.07 ± 0.06^{c}	1.2 ^e	0.85 ± 0.05	14.0 \pm	3.9 ± 0.3
				1.1	
St. 15		1.5 ^f	0.80 ± 0.05	$\textbf{7.4} \pm \textbf{0.6}$	2.6 ± 0.1
St. 12	$0.09\pm0.05^{\text{c}}$	1.0 ^e	0.75 ± 0.05	9.0 ± 0.3	$\textbf{2.3} \pm \textbf{0.2}$

 $^{^{\}rm a}$ Proximal (Type 1) sediment accumulation rates using $^{210}{\rm Pb}$ from Corbett et al., 2006.

^b Distal (Type 3) sediment accumulation rates using ²¹⁰Pb from Corbett et al.,

^c From ²¹⁰Pb measurements from Yeager et al., 2004 (stations MT3 and S36).

 $^{^{\}rm d}\,$ TOC% St. 2 and St. 13 values from Waterson and Canuel, 2008 (stations 80 m and H9).

^e % OC from Morse and Beazley, 2008 (stations MT3 and HiPro).

^f %POC from Zhuang et al., 2019 (Taylor Energy Site).

^g Average porosity and standard deviation over entire core, porosity profiles in supplemental material.

OPD and DOU represent mean values from two ex situ profiles, except for St.
 2 and 13 which were profiled once and St 2b which consisted of two in situ profiles.

i See methods section for calculations.

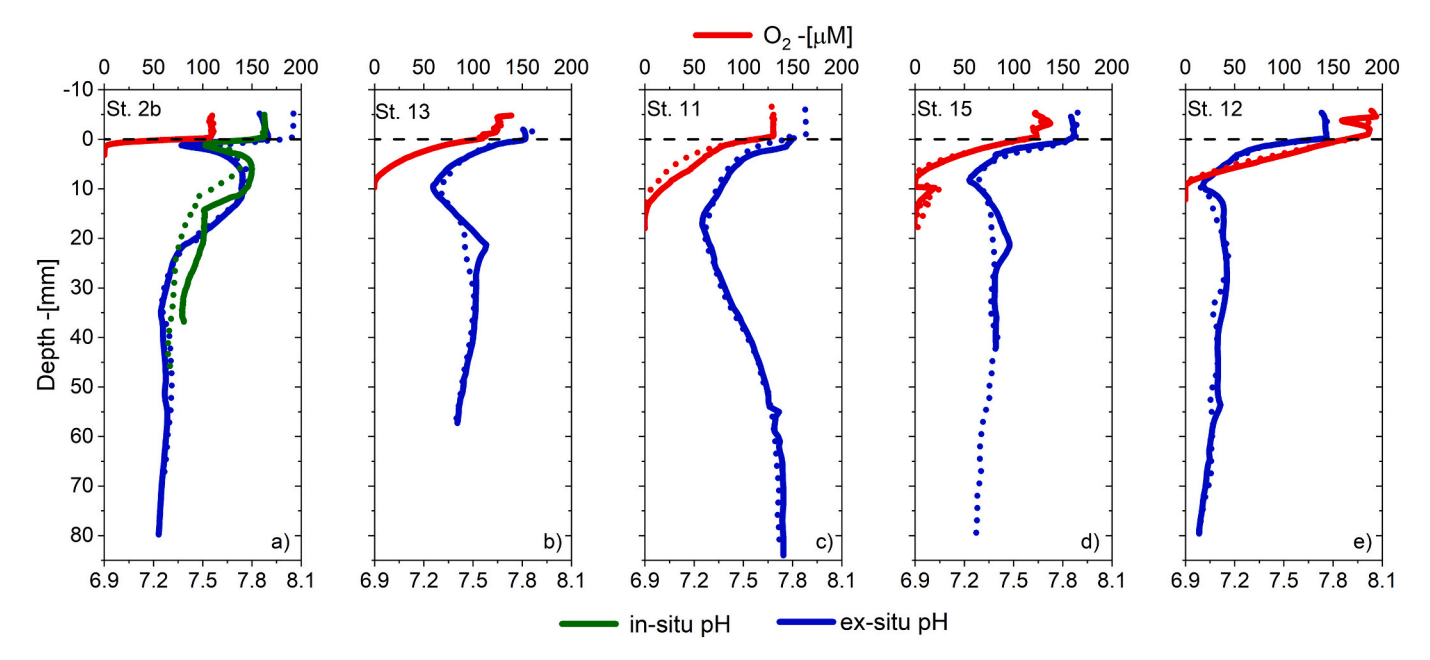


Fig. 2. O_2 (red) and pH (green and blue) microprofiles in sediment cores along the western (St. 2, St. 13 and St. 11) and eastern transects (St. 15, St. 12). Replicate profiles are indicated by solid and dotted lines. Oxygen profiles at St. 2b were collected in situ, while all others were collected ex situ after core collection. The pH profiles at St. 2b were collected both in-situ with a benthic lander (pH-green) and ex situ in sediment cores (blue). The sediment water interface (depth = 0 mm) is indicated by the dashed horizontal line. (For interpretation of the references to color in this figure legend, the reader is referred to the web version of this article.)

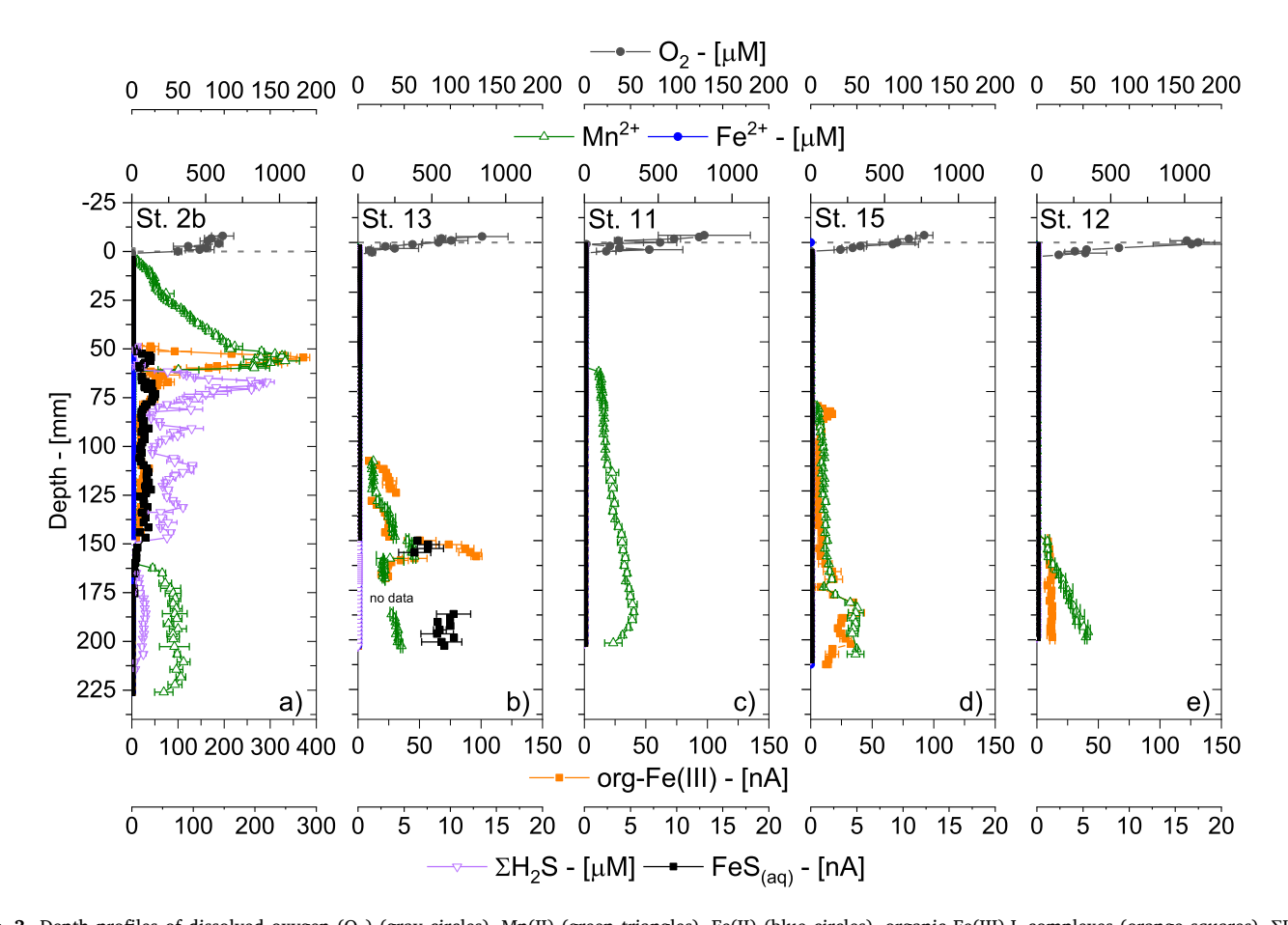


Fig. 3. Depth profiles of dissolved oxygen (O_2) (gray circles), Mn(II) (green triangles), Fe(II) (blue circles), organic Fe(III)-L complexes (orange squares), ΣH_2S (purple down triangles) and FeS_{aq} (black squares) detected voltammetrically in the sediments of: St. 2b (a, b); St. 13 (c, d); St. 11 (e, f); St. 15 (g, h); and St. 12 (i, j). The sediment water interface is indicated by the dashed horizontal line. Note the different scales at St. 2b where concentrations and current intensities were much higher compared to the other stations. Error bars represent the standard deviations of at least triplicate voltammetric measurements at the same location. (For interpretation of the references to color in this figure legend, the reader is referred to the web version of this article.)

displayed the same trend, with an abrupt decrease in pH within the first 1-1.5 cm below the SWI to minimum pH values ranging from 7.0-7.3 followed by a rebound to relatively constant values between 7.0 and 7.8 at depth (Fig. 2). At St. 2b, the pH profile followed a similar trend, however, the pH decrease occurred within a few millimeters (versus centimeters at the other stations) from the SWI. Furthermore, the pH decreased again after the initial rebound in pH around 10 mm and remained at its lowest value (i.e., pH 7.2) below 30 mm in the profile (Fig. 2). Little to no differences were observed between ex situ and in situ oxygen and pH microprofiles (Fig. 2), confirming the integrity of the sediment cores collected during this study. Sediment porosity ranged from 0.86 to 0.95 in surface sediments, decreased by 0.1-0.15 units within the top 50-100 mm, and remained relatively constant at depth (Fig. S1) with average values ranging from 0.75 to 0.87 (Table 2). Overall, stations along the eastern transect displayed lower porosities and steeper decreases in porosity with depth compared to the western transect (Fig. S1), indicative of more significant inputs of fine-grained sediments along the western transect. At each station, the water content of the different sections decreased with depth, suggestive of increased compaction.

3.2. Voltammetric depth profiles of redox species

Dissolved oxygen measured by Au/Hg microelectrodes also decreased rapidly with depth (Fig. 3) but OPDs, although increasing with water depth, were 3-6 mm shallower than detected with the amperometric microelectrodes. At St. 2b, pore water Mn²⁺ concentrations uniformly increased immediately below the sediment water interface (SWI) to a maximum concentration of 1039 \pm 96 μM at 56 mm. Mn²⁺ concentrations then rapidly decreased to below detection limits at 62 mm, and reappeared below 165 mm albeit in lower concentrations (ranging from 141 to 351 $\mu M).$ Although Mn^{2+} concentrations also increased with depth to concentrations ranging between 295 and 347 μM at St. 13, 11, 15, and 12, the onset of Mn^{2+} production was detected much deeper at 103, 65, 82, and 150 mm below the SWI, respectively (Fig. 3). In comparison, Fe²⁺ concentrations remained below detection limits throughout each core, even though org-Fe(III) was detected in all cores except at St. 11. At St. 2b, a strong peak in org-Fe(III) was observed (372 \pm 14 nA maximum) that coincided with the \mbox{Mn}^{2+} peak and progressively decreased to below detection limit at 150 mm. At St. 13, org-Fe(III) was produced between 110 and 146 mm to approximately 20 nA and abruptly increased to 96 \pm 5 nA at 156 mm followed by a decrease to below detection limit within 30 mm. Across the eastern transect, org-Fe(III) was detected in much lower current intensities. At Station 15, org-Fe(III) was produced at 82 mm in low current intensities (ca. 5 nA) and increased to a maximum of 37 \pm 6 nA at depth, whereas org-Fe(III) appeared at 151 mm at St. 12 and remained low deeper (9-12 nA). Dissolved ΣH_2S was only detected at St. 2b, where it was produced below 49 mm and reached a maximum of 219 \pm 14 μM at 67 mm before decreasing regularly to below detection limit at 214 mm. Molecular clusters of FeS (FeS_(a0)) were also detected just above the onset of ΣH_2S production (50 mm) at St. 2b, although their current intensities remained relatively low (3-38 nA) across the profiles and decreased to below detection limit at 178 mm. Finally, FeS(aq) was also detected in low current intensities (max 10 \pm 2 nA) below 150 mm at St. 13, but remained below detection limit at all other stations (Fig. 3).

3.3. Pore water profiles of carbon respiratory products, sulfate, and dissolved metals

Depth profiles of the main redox species reflected the intensity of respiratory processes as revealed by DIC, TA, ΣPO_4^{3-} , and NH $_7^+$ profiles. DIC, TA, ΣPO_4^{3-} , and NH $_7^+$ concentrations increased from the SWI to maxima at depth at all stations, but maximum concentrations decreased with increasing water depth in the order St. 2b (Fig. 4 a₁) >> St. 13 (Fig. 4 b₁) > St. 11 (Fig. 4 c₁). In the eastern transect, DIC, ΣPO_4^{3-} , and

TA did not vary throughout the core at St. 15 (Fig. 4 d₁), indicating little respiratory activity relative to the other stations. In turn, slight increases in DIC, TA, ΣPO_3^{4-} , and NH_4^+ concentrations with depth were observed at St. 12 (Fig. 4 e₁). Sulfate concentrations decreased regularly from 29.9 \pm 0.5 to 21.3 mM at 500 mm at St. 2b (Fig. 4 a₂), only slightly to 26.7 \pm 1.13 mM between 365 and 525 mm at St. 13 (Fig. 4 b₂), and remained relatively constant throughout the profiles at the other stations (Fig. 4 c₂, d₂, and e₂). With respect to the dissolved nitrogen species, NO $_3^-$ concentrations were highest in the bottom waters (ranging between 12 and 31 μ M), decreased rapidly within the first 10–20 mm to approximately 1–5 μ M, and remained relatively constant around these values at depth (Fig. 4 a₂, c₂, d₂, and e₂) as observed previously (Zhuang et al., 2019). In turn, NO $_2^-$ concentrations remained below 5 μ M throughout each core (Fig. 4).

St. 2b displayed the highest Mn_d concentration in the overlying water (12.2 \pm 0.2 $\mu M)$ of all stations (1.7 \pm 0.4 μM at St. 13 and < MDL at St. 11, St. 15, and St. 12) (Fig. 4 a₃, b₂, c₃, d₃, e₃), indicative of a benthic flux as observed by the voltammetric measurements (Fig. 3a). At each western transect station, Mn_d was produced immediately below the SWI and generally displayed a subsurface peak with a maximum concentration ranging between 239 and 400 µM, the position of which increased with depth across the continental slope (10 mm at St. 2b, 43 mm at St. 13, and 127 mm at St. 11) (Fig. 4 a₃, b₃, c₃). Below this peak, Mn_d concentrations decreased to a minimum of approximately 100 μM at 600 mm at St. 2b, whereas it rebounded below 108 mm to a maximum of 277 \pm 6 μM at depth at St. 13 and slightly decreased to a minimum of $191\pm2~\mu\text{M}$ at depth at St. 11. The Mn_d profile at the deepest station of the eastern transect (St. 12), displayed a similar profile as the deepest station of the western transect (St. 11), with increase in Mnd to a maximum of 317 \pm 1 μM at 75 mm but only a slight decrease in concentration with depth (Fig. 4 d₃). Atypical to all other stations, Mn_d concentrations at St. 15 did not display a peak, rather concentrations remained relatively low and gradually increased to 73 \pm 2 μM at 215 mm followed by a decrease in concentration deeper (Fig. 4 e3).

Overall, pore water Fe²⁺ concentrations were lower than pore water Mnd and Fe(III)d concentrations in all cores, suggesting sediments across the continental slopes were suboxic. Although a shallow Fe²⁺ peak (max. $62 \pm 0.6 \,\mu\text{M}$ at 90 mm) was present at St. 2b (Fig. 4 a₃), pore water Fe²⁺ was present in low concentrations (0–15 μ M) throughout the cores of all other stations (Fig. 4 b₃, c₃, d₃, e₃), reflecting what was found with Au/Hg voltammetric microelectrodes (Fig. 3). Station 2b displayed a large Fe(III)_d peak (253 \pm 1.3 μ M) over the first 100 mm of sediment that coincided with the org-Fe(III) peak measured by voltammetry (Fig. 3a) and was accompanied by small increases in Fe2+ measured voltammetrically (Fig. 3a) and pore water Fe²⁺ (Fig. 4 a₃). In the deeper stations along the western transect, the onset of Fe(III)_d production was located at greater depths of 34 and 144 mm at St. 13 and St. 11, and concentrations increased gradually with depth to concentrations of 128 \pm 1.0 and 92 \pm 1.5 μ M respectively (Fig. 4 b₃, c₃). Although org-Fe(III) voltammetric signals did not match the Fe(III)_d profiles at St. 13 and 11, likely due to the highly localized voltammetric measurements compared to the longitudinally-averaged pore water Fe(III)_d concentrations in heterogeneous sediments, org-Fe(III) current intensities were similarly higher at St. 13 compared to St. 11. Along the eastern transect, two subsurface peaks in Fe $^{3+}$ with maximum concentration of 129 \pm 2.1 and $398 \pm 6.3~\mu M$ were found over the first 50 mm and between 200 and 300 mm at St. 15 (Fig. 4 d₃) that generally matched the org-Fe(III) voltammetric profile (Fig. 3d). A gradual increase in Fe³⁺ concentration with depth to $90 \pm 0.6~\mu\text{M}$ was observed at St. 12 (Fig. 4 e_3) that was reflected by the general increase in org-Fe(III) below 150 mm (Fig. 3e).

3.4. Solid manganese, iron, and sulfur profiles

At St. 2b, the highest reactive Mn concentration in the solid phase (20.7 \pm 0.4 $\mu mol~gdw^{-1})$ was present within the first 7 mm of the sediment and included 2.7 \pm 0.1 $\mu mol~gdw^{-1}$ of Mn(III/IV) oxides (Fig. 4

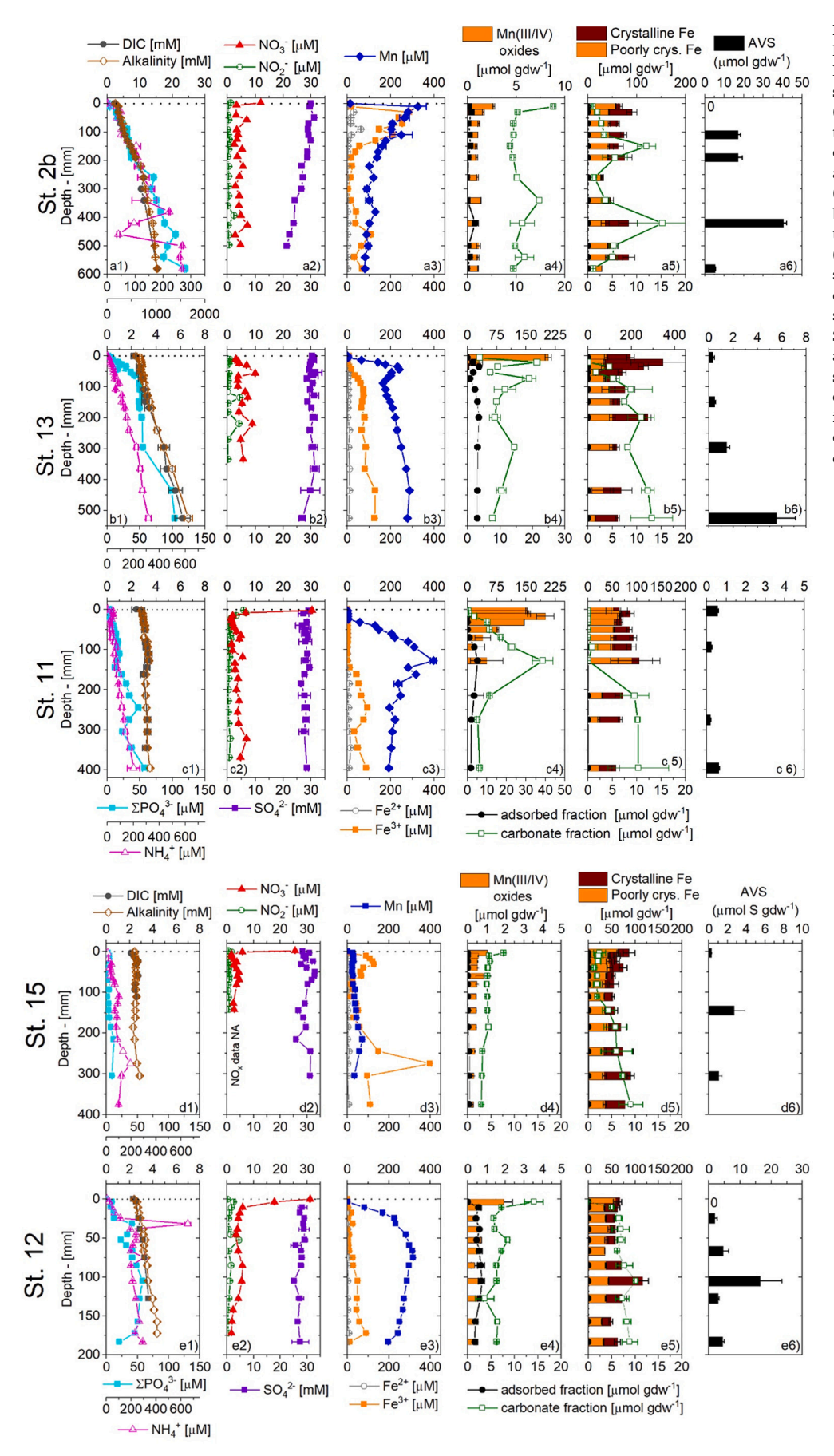


Fig. 4. Depth profiles of DIC, total alkalinity (TA), ΣPO_4^{3-} , and NH_4^+ (first panel), NO₃, NO₂, and SO₄²⁻ (second panel), dissolved Mn(II), Mn(III), Fe(II), and Fe(III)_d (third panel), total solid Mn and Fe partitioned as adsorbed, carbonate, noncrystalline, and crystalline phases (fourth and fifth panels), and 'acid volatile sulfides' (sixth panel) at: St. 2b (a₁-a₆); St. 13 (b₁ b_6); and St. 11 (c_1 - c_6) along the western transect and at: St. 15 (d₁-d₆); and St. 12 (e₁-e₆) along the eastern transect. The sediment water interface is indicated by the dashed horizontal line. Note the change in scale of alkalinity, DIC, ΣPO_4^{3-} , and NH_4^+ at St. 2b in comparison with the other stations as well as the change in scale of Mn and Fe solid phase speciation and AVS between each station to observe general trends. '0's in the sixth panels represent AVS analyses of surface sediments that were below detection limit.

 a_4). The remainder of the core consisted of reactive Mn concentrations ranging between 10 and 16 µmol gdw⁻¹, the majority of which (8–14 μmol gdw⁻¹) was in carbonate-bound Mn²⁺ (80–91%), a smaller fraction (0.9–1.6 μ mol gdw⁻¹, 6–12%) as Mn(III/IV) oxides, and a much smaller adsorbed Mn²⁺ fraction (0–1.6 µmol gdw⁻¹, 0–11%). The distribution of solid phase Mn was typically similar at stations St.13 and St. 11, with an enrichment of Mn(III/IV) oxides at the surface (207 \pm 8.0 and 151 \pm 1.9 μ mol gdw $^{-1}$ respectively) that rapidly decreased to 1.2 \pm $0.2~\mu mol~gdw^{-1}$ at 53 mm at St. 13 but only progressively to 1.3 ± 0.2 μmol gdw⁻¹ at 215 mm at St. 11 (Fig. 4 b₄, c₄). At both stations, carbonate-bound Mn²⁺ represented the dominant fraction (56-86% at St. 13 and 0.5-71.3% at St. 11) across the sediment column (Fig. S2) and increased in concentrations below the Mn(III/IV) oxide maximum. This increase, however, was much more rapid at St. 13 (approx. 1.3 µmol gdw⁻¹ per mm on average between 7 and 20 mm) than at St. 11 (approx. 0.3 μmol gdw⁻¹ per mm on average between 3 and 127 mm). Adsorbed Mn²⁺, which was rapidly produced below 20 mm at St. 13 and much more progressively below 70 mm at St. 11 (Fig. 4 b₄ and c₄), remained relatively low in concentration at both stations (0.9–3.7 µmol gdw⁻¹ at St. 13 and 1.2–5.2 μ mol gdw⁻¹ at St. 11), not exceeding 30% of the sum of Mn (Fig. S2). Along the eastern transect, Mn(III/IV) oxides and carbonate Mn²⁺ displayed similar trends with the highest Mn(III/IV) oxide concentrations found at the sediment surface (1.1 \pm 0.1 μ mol gdw⁻¹ at St. 15, 1.9 \pm 0.5 μ mol gdw⁻¹ at St. 12) but <1 μ mol gdw⁻¹ Mn(III/IV) oxides across the rest of the sediment column. Similarly, the carbonate Mn²⁺ fraction, though dominating the solid phase speciation at both St. 15 and St. 12 (Fig. S2), was highest at the surface (7.63 \pm 0.09 at St. 15, 14.12 ± 2.03 at St. 12) and below 5 and 8 $\mu mol\ gdw^{-1}$, respectively, across the remainder of the sediment column (Fig. 4 d4, e4). Interestingly, the difference in Mn solid phase speciation between St. 15 and St. 12 manifested in the adsorbed fraction which increased only to $0.3 \mu mol$ gdw⁻¹ at 245 mm at St. 15, in contrast to St. 12 where adsorbed Mn²⁺ was detected as high as 1.5-3.0 μmol gdw⁻¹ between 10 and 183 mm (Fig. 4 d₄,e₄, Fig. S2).

The distribution of total reactive Fe in St. 2b sediment was relatively homogeneous with depth and included relatively high concentrations of poorly crystalline (30–55 μ mol gdw⁻¹ or 40–100% of total reactive Fe) and crystalline (0–47.7 μ mol gdw⁻¹ or 0–51% of total reactive Fe) Fe (III) (Fig. 4 a₆, Fig. S2), and generally low carbonate-bound Fe²⁺ (< 10%) (Fig. 4 a₅, Fig. S2). The distribution of total reactive Fe was more variable at St. 13 (Fig. 4 b₅, Fig. S2), where the surface sediment (0-53 mm) was depleted in poorly crystalline Fe(III) oxides (36-83 µmol ${\rm gdw}^{-1}$ or 29 \pm 10% of total reactive Fe) and enriched in crystalline Fe (III) oxides (112–269 $\mu mol\ gdw^{-1}$ or 57–77%), and the deep sediment was enriched in poorly crystalline Fe(III) oxides (μmol gdw⁻¹ or %) and depleted in crystalline Fe(III) oxides (34–112 μmol gdw⁻¹ or 22–79%). Although low at the surface (0–4.4 μ mol gdw⁻¹ or 0–1.6%), carbonatebound Fe^{2+} concentrations increased at 73 mm to reach 5–13 μmol gdw^{-1} or 3.8–8.7% of total reactive Fe between 73 and 525 mm (Fig. 4 b₅, Fig. S2). The inverse trend was apparent at St. 11 (Fig. 4 c₅), where poorly crystalline Fe(III) oxides rapidly increased below the SWI to 90 μmol gdw⁻¹ at 20 mm and constituted the majority of total reactive Fe (80–93%, Fig. S2), then decreased progressively to 22.8 \pm 2.5 μmol gdw⁻¹ at depth. Although generally low at St. 11 (34–43 µmol gdw⁻¹, Fig. 4 c₅), crystalline Fe(III) oxides were proportionally lower than the poorly crystalline Fe(III) oxides fraction in surficial sediment (< 20%) but represented the dominant fraction of total reactive Fe in the deep sediment (50-56%) with a small contribution from the carbonate fraction (9.6–10.4 μ mol gdw⁻¹ or ~12%) between 215 and 395 mm (Fig. 4 c₅, Fig. S2). On the eastern transect, poorly crystalline and crystalline Fe (III) oxide distributions were similar at both stations: The first 4 mm consisted mainly of poorly crystalline Fe(III) oxides (63.1 \pm 2.0 and $58.5 \pm 4.8 \, \mu mol \, gdw^{-1}$ at St. 15 and St. 12) (Fig. 4 d₅, e₅). Below the first section, poorly crystalline Fe(III) oxides constituted slightly more than half (58 \pm 37% at St. 15 and 55 \pm 15% at St. 12) of total reactive Fe (Fig. 4 d₅,e₅, Fig. S2). On the other hand, differences in the carbonate

fraction were evident along the eastern transect, where carbonate-bound Fe^{2+} concentrations increased from 2.4 \pm 1.2 at the surface to $9.03\pm2.6\,\mu\text{mol gdw}^{-1}$ at depth at St. 15, whereas the carbonate fraction averaged 7.4 \pm 1.5 $\mu\text{mol gdw}^{-1}$ below the first 7 mm at St. 12 (Fig. 4 d₅, e₅).

At all stations, AVS concentrations were low in the top 3-10 mm of sediment, ranging from below detection limit to the highest value of $0.56 \pm 0.05 \; \mu mol \; S \; gdw^{-1}$ at St. 11 (Fig. 4 a₆, b₆, c₆, d₆ and e₆). The highest AVS concentrations throughout the core were found in St. 2b, with a peak in concentration of 40.3 \pm 1.7 μ mol S gdw⁻¹ at 42 mm, followed by the lowest concentration measured in the core of 5.3 \pm 0.4 μmol S gdw⁻¹ at 580 mm (Fig. 4 a₆). AVS concentrations at St. 13 were generally low but increased from 0.35 \pm 0.12 μ mol S gdw⁻¹ at the surface to 5.6 \pm 1.6 μ mol S gdw $^{-1}$ at the bottom of the core (525 mm) (Fig. 4 b₆). AVS concentrations were even much lower at Station 11, remaining below 1 μmol S gdw⁻¹ throughout the core (Fig. 4 c₆). Along the eastern transect, AVS concentrations were also low at St. 15, with a maximum concentration of 2.7 \pm 1.13 μ mol S gdw⁻¹ at 145 mm, whereas AVS concentrations were generally higher and ranged between 1.8 and 4.6 µmol S gdw⁻¹ at St. 12, with a maximum concentration of $16.4 \pm 7.0 \ \mu mol \ S \ gdw^{-1}$ at 105 mm (Fig. 4 d₆ and e₆).

4. Discussion

4.1. Intensity of carbon remineralization and main diagenetic pathways from the continental shelf to the slope

Although bottom waters were oxygenated, St. 2b, 13, 11, and 15 displayed lower percent saturations (44-48%) in comparison to those previously found (55-100%) in the nGoM shelf and slope region during August-September 2006 (Hu et al., 2011). Low oxygen saturation in the bottom waters could be caused by upwelling of O2-depleted waters, respiration in the water column, or O2 consumption by the sediments along with low vertical mixing rate due to limited winds or absence of storm events. As the surface area of the hypoxic zone during the summer of 2017 was the largest ever recorded in the northern Gulf of Mexico (22,720 km²) (Rabalais and Turner, 2017), it is likely that strong respiration in the water column and low vertical mixing conditions were responsible for the depleted O2 levels in the overlying waters. The highest DOU rate was measured on the western transect and decreased from 13.8 mmol $m^{-2} d^{-1}$ on the shelf (St. 2b) to 3.6 on the slope (St. 13) and 3.9 mmol m $^{-2}$ d $^{-1}$ at the bottom of the slope (St. 11) (Table 2). DOU rates along the eastern transect also decreased with distance from the shelf but were about 17 and 42% lower on the slope and bottom of the slope than along the western transect (Table 2). These DOU rates are comparable to sediment community oxygen consumption (Rowe et al., 2008) and DOU rates measured at the deep stations along the continental shelf and slope (Hu et al., 2011). In turn, DOU appears to vary seasonally on the shelf near St. 2b (Lehrter et al., 2012; Rowe et al., 2002). The higher DOU rates and compressed pH profile at St.2b are indicative of intense carbon remineralization and re-oxidation in a thin sediment section near the SWI due to large labile organic carbon deposition from MARS (Table 2). The reactive transport model that optimized respiration rates to reproduce the experimental depth profiles (Fig. 5 and Figs. S3–S6) confirms that aerobic respiration represents the main O₂ consumption process along these continental shelf and slope sediments except at St. 13, where the OPD was much larger than any other station and the contribution of reduced metabolites reoxidation to O₂ removal reaches around 60% (Table 3). Except for St. 2b, where high Mn²⁺ fluxes were calculated ($-1325 \pm 70 \ \mu mol \ m^{-2} \ d^{-1}$), Fe²⁺ and Mn2+ diffusive fluxes across the SWI were either absent or low (Table S9), suggesting most of the reduced metabolites produced during anaerobic respiration processes were buried under the form of sulfide or carbonate minerals in the deep sediment (Fig. 4). In contrast, DIC, NH₄, and even ΣPO_4^{3-} diffused across the SWI (Figs. 4, 6), demonstrating input of nutrients into the overlying waters that may help fuel new primary

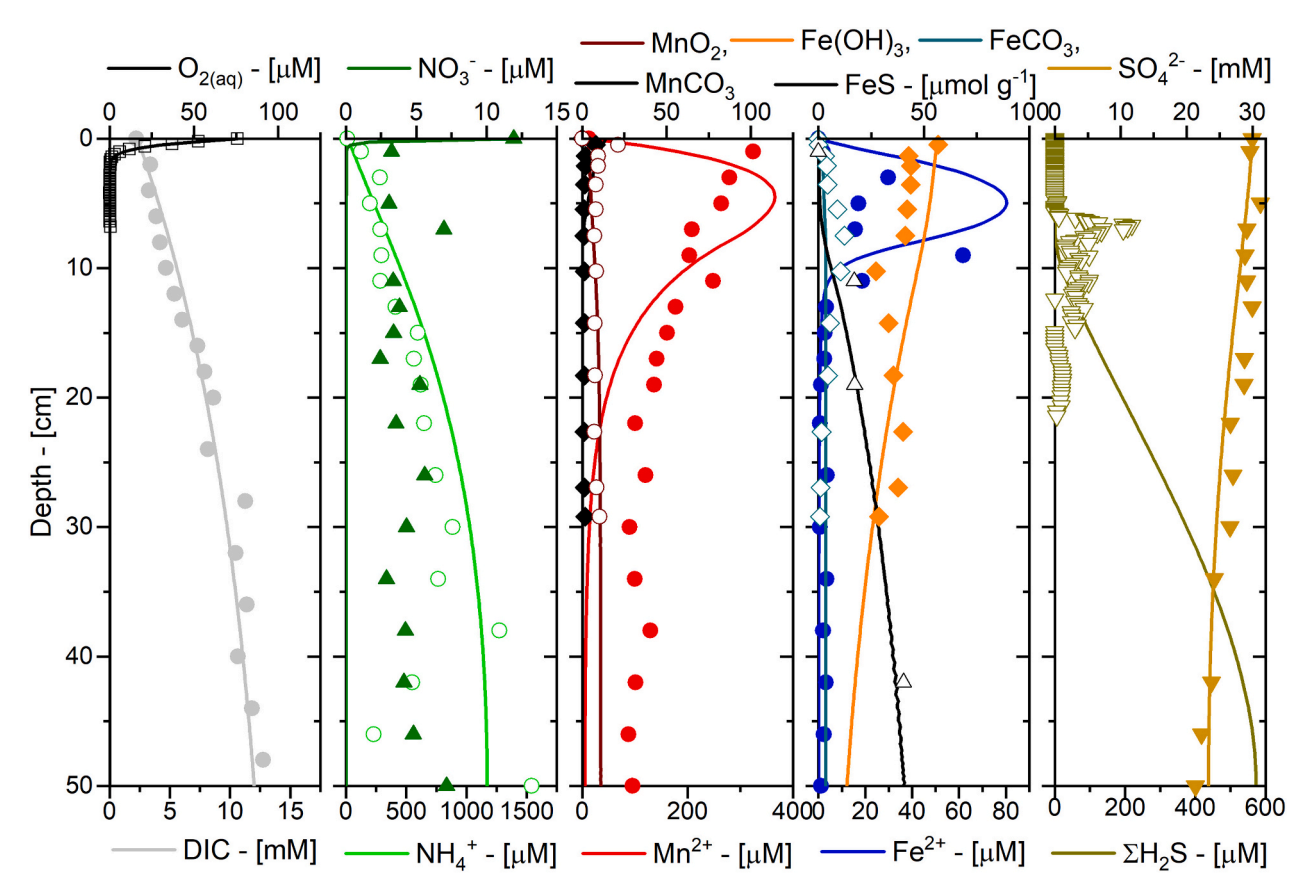


Fig. 5. Example of modeled depth profiles of the main species involved in diagenetic processes at St. 2b (plain lines) compared to experimental depth profiles (scatter points). Only respiration rates (aerobic, denitrification, Mn reduction, Fe reduction, and SO_{4}^{2-} reduction) were optimized to fit the experimental data at steady-state. Rate constants of abiotic processes and biological oxidation of NH_{4}^{+} , $\Sigma H_{2}S$, and Mn^{2+} by $O_{2(aq)}$ were fixed at each station.

Table 3

Percent O₂ consumption by reoxidation of reduced metabolites and relative importance of aerobic respiration, denitrification, Mn(III/IV) oxide reduction, Fe(III) oxide reduction, and sulfate reduction on carbon remineralization processes calculated by the MATSEDLAB reactive transport model at steady-state.

Station	O ₂ Consumption by reduced metabolites (%)	Aerobic respiration (%)	Denitrification (%)	Mn reduction (%)	Fe reduction (%)	SO ₄ ²⁻ reduction (%)	Rate cox (mmol m ⁻² d ⁻¹)
St. 2b	17.7	11.7	15.1	5.3	4.1	63.8	16.5
St. 13	60.5	20.3	24.0	23.7	5.4	26.6	3.6
St. 11	0.6	68.5	16.5	8.9	0.2	5.9	4.5
St. 15	3.6	73.1	19.1	2.8	4.8	0.2	1.8
St. 12	17.4	47.1	17.7	4.4	0.6	30.2	10.3

production (Fig. 6). The trends in flux values indicate a decrease in overall anaerobic carbon remineralization rates from the shelf to the continental slope in agreement with respiration measurements in incubations of Louisiana shelf and slope sediments (Lin and Morse, 1991) and integrated carbon remineralization rates calculated with the reactive transport model (Table 3). Interestingly, the stations in the middle of the slope (i.e., St. 13 for the eastern transect and St. 15 for the western transect) also showed much lower DIC and NH₄ diffusive fluxes (Fig. 6) and integrated carbon remineralization rates (Table 3) than the deepest stations (i.e., St. 11 and St. 12). As riverine inputs of particulate matter extend widely on the slope (Green et al., 2006), these findings suggest the accumulation of particulate material may be transient along the steepest part of the slope (Fig. 1). Integrated carbon remineralization rates calculated with the model are between 20% and 3-4 folds higher than DIC fluxes at the SWI calculated from pore water measurements (Fig. 6), except at St. 11 where carbon remineralization rates are 38% lower. The generally higher carbon remineralization rates than DIC fluxes is attributed to the precipitation of calcium-magnesium carbonate minerals (not determined and not considered in the model), as

precipitation of Fe (Fig. 4 a_4 - e_4) and Mn (Fig. 4 a_5 - e_5) carbonate minerals was observed but their burial fluxes do not significantly remove carbonates from the pore waters (Table S9). In turn, calcium-magnesium carbonate dissolution may be responsible for the missing DIC flux at St. 11. Using mass balance, the missing carbonate precipitation or dissolution flux is estimated to range between 0.2 and 4.5 mmol m⁻² d⁻¹ at all stations, except at St. 12 where the missing flux may reach 7 mmol m⁻² d⁻¹.

The rapid decrease in NO_3^- concentrations below the SWI is attributed to intense denitrification in Gulf of Mexico sediments (McCarthy et al., 2015). Denitrification plays a significant role in the top 2 cm of sediment, suggesting its effect on carbon remineralization processes may be important. Indeed, the reactive transport model ran at steady-state reveals that denitrification constitutes between 15 and 25% of carbon remineralization rates and is more prominent in mid-slope sediments (St. 13 and St. 15) where bottom water NO_3^- concentrations are larger (Table 3). However, these calculations do not account for anaerobic nitrification processes that may explain the low, yet above detection limit, NO_3^- concentrations below the apparent denitrification zone (< 2

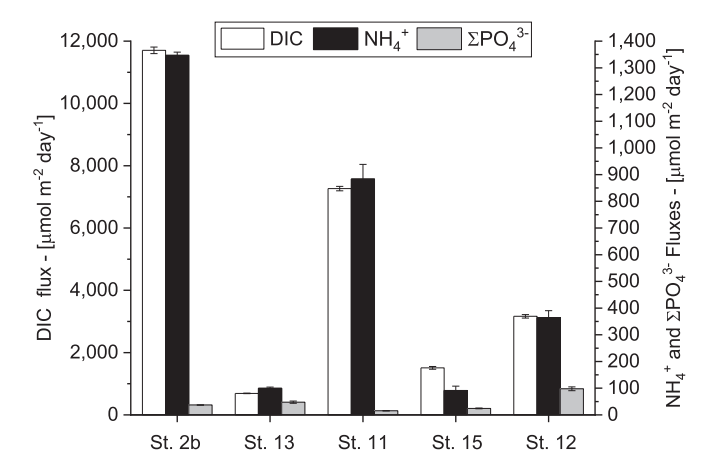


Fig. 6. Diffusive fluxes of DIC, NH $_{+}^{+}$, ΣPO_{4}^{3-} , and SO_{2}^{2-} across the sediment-water interface. Error bars represent the standard deviation extrapolated from porosity.

cm) which would enhance overall denitrification even more. In turn, multiple proxies suggest sulfate reduction is most active on the shelf of the western transect (St. 2b) and decreases in intensity with water depth. First, a significant decrease in sulfate concentrations on the shelf (St. 2b) and mid-slope (St. 13) that was not observed at the bottom of the slope (St. 11), and the detection of ΣH₂S at St. 2b only, provide evidence for sulfate reduction on the upper slope but not in deep sediments. Second, AVS was present throughout the sediment at St. 2b and deep in the sediment at St. 13, and the simultaneous detection of $FeS_{(aq)}$ at these stations indicates active precipitation of FeS (Beckler et al., 2016; Rickard and Luther, 1997; Taillefert et al., 2000; Theberge and Luther, 1997). In contrast, AVS was only observed in small concentrations and $FeS_{(aq)}$ was not detected at St. 11 (Fig. 3). Finally, ΣH_2S either reduce Mn (III/IV) oxides (Herszage and Dos Santos Afonso, 2003) and Fe(III)_d or precipitate Fe²⁺ rapidly (Taillefert et al., 2000). Thus, the low Mn(III/ IV) oxide concentrations below 5 cm (St. 2b and 13), generally low Fe (III)_d concentrations and org-Fe(III) current intensities below 10 cm (St. 2b) and 20 cm (St. 13), and decreasing Fe²⁺ concentrations with depth (St. 2b) (Figs. 3 and 4) present additional evidence that sulfate reduction is most active in shelf and upper slope sediments of the western transect. Comparatively, Fe(III)_d concentrations and org-Fe(III) current intensities were much lower or below detection limit at St. 11, whereas Mn (III/IV) oxides and Fe²⁺ concentrations declined at deeper depths in the sediment, suggesting that sulfate reduction is much less significant deeper along the slope. In contrast to the western transect, sulfate reduction appears insignificant along the eastern transect mid-slope sediment (St. 15) as sulfate concentrations did not decrease significantly (Fig. 4 d₂), in agreement with previous studies on the Louisiana shelf (Zhuang et al., 2019) and slope (Lin and Morse, 1991). Neither $FeS_{(aq)}$ nor ΣH_2S were detected (Fig. 3d), org-Fe(III) (Fig. 3d) and/or Fe³⁺ (Fig. 4 d₃) were observed at depth, and AVS concentrations were much lower (Fig. 4 d₆), in agreement with visual inspection of the cores which did not reveal any black FeS(s) in sediments at St. 15. In turn, sulfate reduction appeared much more important in the deep sediments of the eastern transect (St. 12). Although FeS_(aq) and Σ H₂S (Fig. 3e), indicative of active bacterial activity, were not detected, sulfate decreased noticeably in the first 12 cm (Fig. 4 e₂), Fe(III)_d concentrations remained low, Fe²⁺ decreased deep in the sediment (Fig. 4 e₃), and AVS concentrations were much higher than in the mid-slope sediments (Fig. 4 e₆) as corroborated by visual FeS patches at St. 12 (Fig. 1). The reactive transport model confirms that the contribution of sulfate reduction to carbon remineralization rates (Table 3) is highest on the shelf of the western transect (64% at St. 2b) and decreases as water depth increases (27% at St. 13 and 6% at St. 11). These calculations also demonstrate that the contribution of sulfate reduction to carbon

remineralization processes is low along the slope of the eastern transect (0.2% at St. 15) but much higher in the deep sediments (30% at St. 12).

Simultaneously, geochemical evidence suggests microbial Mn(III/ IV) and Fe(III) oxide reduction are active in the surface sediments of St. 2b and 13 and relatively important across the sediment column at St. 11 and 15, but much less at St. 12 (Fig. 3, 4). The presence of org-Fe(III) and Fe(III)_d indicates Σ H₂S was not produced significantly in the top 5 cm at St. 2b (Figs. 3a and 4c), top 15 cm at St. 13 (Figs. 3b and 4h), and across the profiles at St. 11 and 15 (Fig. 3c and d, Fig. 4 c₃-d₃). The formation of org-Fe(III) at depths much deeper than oxygen penetration and the build-up of Fe²⁺ in the pore waters (Fig. 4 a₃-c₃ and e₃) before the decrease in sulfate concentration also suggests microbial Fe(OH)₃ reduction was active at depth in these sediments (Beckler et al., 2016; Taillefert et al., 2017). In turn, the absence of org-Fe(III), much lower Fe (III)_d concentrations, and decrease in Fe²⁺ with depth below 80 mm at St. 12 suggest that sulfate reduction was more prominent at the deepest station of the eastern transect. Although the reactive transport model indicates that Mn(III/IV) oxide reduction contributes between 5 and 24% of carbon remineralization rates at St. 2b and 13 compared to 9% at St. 11 (Table 3), the contribution of microbial Fe(III) oxide reduction is much smaller at these stations (< 6% of carbon remineralization rates). These findings are explained by the shallow location of the sulfate reduction zone on the shelf at St. 2b (Fig. 5), mid-slope at St. 13 (Fig. S3), and bottom of the slope at St. 11 (Fig. S4) that compresses the microbial metal reduction zone against the SWI and therefore favors microbial Mn (IV/III) reduction and abiotic Fe(III) oxides reduction by ΣH₂S with eventual precipitation of MnCO3 and FeS minerals. Along the eastern transect, microbial metal reduction rates are much lower, and the anaerobic respiration of carbon is mainly driven by denitrification (19% at St. 15 and 18% at St. 12) with minor contribution by microbial Mn (III/IV) oxide reduction (< 5%). These findings corroborate with the generally low sediment deposition rates predicted across the slope at this location (Xu et al., 2011).

4.2. Dissolved metal transport mechanism and enrichment of Mn(III/IV) oxides on the Louisiana slope

The Mississippi River supplies a large load of particulate material during its high discharge period from the winter to early spring that is eventually deposited on the Louisiana shelf (Corbett et al., 2006; Corbett et al., 2004; Devereux et al., 2019). These sediments form mobile muds that are often remobilized by physical mixing generated by tidal currents or storms (Sampere et al., 2011). This process eventually sorts material by size, morphology, or composition (McKee et al., 2004), transports terrestrial organic carbon (Waterson and Canuel, 2008) and inorganic material (Trefry and Presley, 1982) to the deep sediment, and may increase diagenetic reactivity by a priming effect (Bianchi, 2011). An enrichment of Mn(III/IV) oxides is observed at the sediment surface of St. 13 and more particularly St. 11, but not St. 2b, nor along the eastern transect (St. 15 and 12) where Mn(III/IV) concentrations remain low across the sediment (Fig. 4 a₄-e₄). Indeed, the total reactive Mn:Fe ratios (log of the sum of reactive Mn(II/IV) oxides, adsorbed Mn²⁺, and carbonate-bound Mn²⁺ relative to dithionite-extracted Fe) in the top 5 cm of St. 13 and in the top 25 cm of St. 11 are far greater (Fig. 7) than the total reactive Mn:Fe ratios at St. 2b, 15, and 12 (Fig. 7) which remain relatively constant with depth. Surface enrichment in Mn(III/IV) oxides such as that observed at St. 13 and 11 is commonly reported in marine sediments along water depth gradients (Aller, 1994; Law et al., 2009; Mouret et al., 2009; Sundby et al., 1981; Trefry and Presley, 1982; Wade et al., 2008). Such feature is attributed to the diffusive flux of Mn²⁺ formed at sediment depth in reduced conditions to the oxic zone and eventual heterogeneous reoxidation by oxygen (Sundby and Silverberg, 1985; Trefry and Presley, 1982). As the oxidation of Mn²⁺ is generally slow in sediments, Mn(III/IV) oxides are not recycled efficiently (Richard et al., 2013). Rates of Mn²⁺ oxidation, however, are enhanced by bioirrigation which increases both the penetration of dissolved

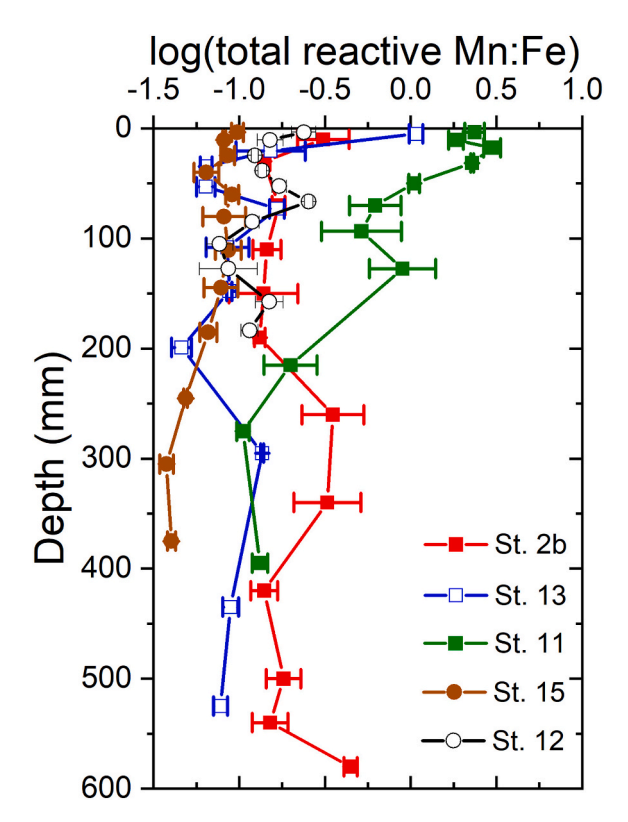


Fig. 7. Depth profiles of total reactive Mn to Fe ratios (logarithmic scale) at St. 2 (red), St. 13 (blue), and St. 11 (green) along the western transect and St. 15 (brown) and St. 12 (black) along the eastern transect. Total reactive Mn includes the sum of reactive Mn(III/IV) oxides, adsorbed $\rm Mn^{2+}$, and carbonate-bound $\rm Mn^{2+}$, whereas total reactive Fe was quantified by the dithionite extraction. (For interpretation of the references to color in this figure legend, the reader is referred to the web version of this article.)

oxygen into the sediment (Aller and Aller, 1998) and the exchange of Mn²⁺ with the overlying waters (Boudreau, 1997). In turn, Mn²⁺ oxidation rates are decreased by the precipitation of MnCO₃ minerals in pore waters (Duckworth and Martin, 2004). Evidence of bioirrigation exists in the oxygen profile at St. 15, where a pocket of oxygen was detected below the OPD (Fig. 2) and has been documented in the vicinity of the slope stations (Xu et al., 2014). Low adsorbed Mn²⁺ concentrations were observed at depth in cores along both transects (Fig. 4 a₄-e₄, Fig. S2). Additionally, adsorbed Mn²⁺ was absent in the surface sediments, likely due to enhanced Mn²⁺ oxidation in the oxic zone by surface catalyzed reactions on Fe(III), Al, and Si oxide surfaces (Davies and Morgan, 1989; Lan et al., 2017). In the shelf and mid-slope sediments of the western transect (St. 2b and St. 13), microbial Mn(IV/III) reduction and reduction of Mn(IV) oxides by $\Sigma H_2 S$ generate a high upward flux of Mn²⁺ to the sediment surface (Fig. 4 a₃-b₃) that leads to a significant diffusive flux across the SWI at St. 2b and small, but detectable at St. 13 (Table S9), even though a significant fraction of Mn²⁺ is immobilized under the form of carbonate minerals (Fig. 4 a₄-b₄ and Fig. S2). In fact, the diffusive flux of Mn²⁺ at the SWI is much larger than the average burial fluxes of MnCO3 at St 2b, suggesting that the shelf station represents an important source of Mn²⁺ to the overlying waters. Compounded by the low dissolved O₂ concentrations of the overlying waters at St. 2b (Table 1), model calculations demonstrate that O₂ consumption by reoxidation of reduced metabolites in the sediment is relatively small (< 20%) except at St. 13 (Table 3). As a result, Mn_d is able to reach the bottom waters at the shelf station (Table S9) where it is likely removed by particle adsorption (Trefry and Presley, 1982), oxidized heterogeneously (Davies and Morgan, 1989), then eventually transported by mobile muds and deposited along continental slope sediments (St. 13 and St. 11). Ultimately, these Mn-enriched materials generate a Mn

'conveyor belt' from the shelf to the bottom of the slope, as observed with Mn and Fe in a variety of continental margins (e.g., Lyons and Severmann, 2006; Scholz et al., 2011 and 2013; Jilbert and Slomp, 2013; Scholz et al., 2019; Lenstra et al., 2020). Although the upward diffusive flux of Mn²+ was not significantly lower at St. 11 (136 \pm 10 μ mol m²- d^{-1}) than the mid-slope sediment (172 \pm 17 μ mole m²- d^{-1} at St. 13), Mn²+ did not reach the SWI (Fig. 4 c³ and Table S9) due to the enhanced thickness of the Mn²+ oxidation zone, as evidenced by the deeper OPD, pH minimum (Fig. 2), and position of the dissolved Mn peak (Fig. 4 b³-c³).

4.3. Differential Iron and Mn cycling

The pore water and solid phase speciation of Mn and Fe as a function of depth in these sediments is consistent with the predictions of the thermodynamic redox ladder regarding the dynamics of Fe and Mn redox cycling (Froelich et al., 1979). Whereas Mn²⁺ concentrations were greater than Fe²⁺ in most sediment pore waters studied, the inverse is true in the solid phase (Fig. 4), except for a few depths near the sediment surface at St. 11 where Mn(III/IV) oxides were enriched relative to Fe (III) oxides (Fig. 4 c₄-c₅). Abiotic and biotic Mn(III/IV) oxides reduction are typically faster than Fe(III) oxide reduction (Arnold et al., 1988; Dollhopf et al., 2000; Herszage and Dos Santos Afonso, 2003; Larsen et al., 1998; Lovley and Phillips, 1988; Myers and Nealson, 1988), whereas Mn²⁺ oxidation is much slower than Fe²⁺ oxidation (Stumm and Morgan, 1996; Richard et al., 2013). The large abundance of poorly crystalline (51 \pm 21 μ mol gdw $^{-1}$) and crystalline Fe(III) oxides (46 \pm 45 μ mol gdw⁻¹) throughout each profile, representing about 94 \pm 5% of total reactive Fe in these sediments (Fig. S2) and the low AVS concentrations in all sediments except St. 2b and the deep layers of St. 13 (Fig. 4 a₆-e₆) suggest that these sediments have been exposed to dissolved oxygen. Although bioturbation was not directly assessed, depth profiles of dissolved constituents (e.g., NH₄, DIC) appeared diffusive all the way to the SWI (Fig. 4 a₁-d₁) whereas depth profiles of Fe(III) oxides were not significantly enriched near the SWI (Fig. 4 a₅-d₅), suggesting that bioturbation was not intense at these stations. As evidence for intense bioturbation is lacking, it is likely that exposure to dissolved oxygen occurred during resuspension as mobile muds prior to eventual deposition and accumulation. In contrast to Mn²⁺, however, Fe²⁺ is mostly retained in the sediment (Table S9) either by oxidation near the SWI or precipitation under the form of carbonate or sulfide minerals. These findings are different than the recent Mn (Lenstra et al., 2020) and Fe (Lenstra et al., 2019) conveyer belt observed in the Black Sea, although the benthic flux of these metals from the coastal stations was attributed to intense bioturbation which enhanced the supply of organic matter and dissolved oxygen and stimulated both Fe and Mn reduction close to the SWI.

The data collected in this study immediately at the end of the high discharge period confirm that sedimentary material is transported all the way to the bottom of the slope (St. 11) during the high discharge period and preferentially enriched in Mn(III/IV) oxides relative to reactive Fe. Whereas Mn(III/IV) oxide reduction was intense in these sediments, the reduction of Fe(III) oxides was apparently not significant (i.e., low Fe²⁺, FeCO₃ minerals, and FeS_(s)), providing evidence for the differential kinetics of microbial Mn and Fe reduction in a natural setting. The reactive transport model confirms these findings by demonstrating that the Mn:Fe input flux ratio at the SWI is increased with depth across each transect (Table S8) and metal respiration processes on the slope during that time period were mainly controlled by microbial Mn reduction and not microbial Fe reduction (Table 3). As suggested by thermodynamic calculations (Fig. S7), microbial Fe(III) oxide reduction likely dominates after depletion of the Mn(IV) oxides, which would explain the high concentrations of reduced Fe²⁺ previously observed near St. 12 (Beckler et al., 2016). However, it is not clear whether the stock of Fe(III) oxides is large enough to prevent sulfate reduction from dominating anaerobic respiration processes during the rest of the summer and fall. The enhanced production of carbonates under sulfate reducing conditions (i.e., one mole of SO_4^{2-} reduced produces two moles of carbonate) should at least bury Mn^{2+} , thus preventing its diffusion across the SWI and reducing the efficiency the Mn conveyor belt at the end of the high discharge period. Overall, these findings indicate continental slope sediments exposed to large riverine inputs are highly dynamic systems that may remineralize natural organic matter using different terminal electron accepting processes depending on riverine discharge intensity.

5. Conclusions

The main redox processes involved in the transformation of natural organic matter in RiOMars sediments were investigated along two transects in the northern Gulf of Mexico to examine the effect of particulate material inputs from the Mississippi River plume on diagenetic processes after a high riverine discharge period. Results suggest organic carbon deposition control the intensity of anaerobic carbon remineralization processes and select the dominant anaerobic carbon remineralization pathways. Although sulfate reduction dominates at the shelf station (65 m water depth), microbial Mn reduction appears to represent a significant anaerobic respiration process along the continental slope closest to the Mississippi River plume whereas iron mainly remains under the form of Fe(III) oxides and does not play a major role in carbon remineralization. These findings suggest the differential kinetics of Mn and Fe redox transformations coupled with the high discharge of the Mississippi River during the winter and spring influence carbon remineralization processes on the continental slope. The fast Fe²⁺ oxygenation kinetics near the sediment-water interface and high sedimentation rates maintain iron under the form of Fe(III) oxides and prevent sulfate reduction from being significant, whereas the much slower kinetics of oxygenic oxidation allows diffusion of Mn²⁺ across the sediment-water interface. Exposure to bottom water oxygen and mobile muds typical of deltaic sediments during high riverine discharge likely promote the formation and downslope transport of Mn(III/IV) oxides, forming a Mn 'conveyor belt' that selectively enriches Mn(III/IV) oxides relative to Fe (III) oxides in the deep slope sediment. It is not clear whether the stock of Fe(III) oxides is large enough to prevent sulfate reduction from dominating anaerobic respiration processes over time. The enhanced production of carbonates under sulfate reducing conditions should at least reduce the efficiency of the Mn conveyor belt and efficiently bury this important terminal electron acceptor during the low riverine discharge period. In contrast, the intensity of carbon remineralization processes along the eastern continental slope the farthest from the Mississippi River plume is much lower due to the low organic and lithogenic inputs, and denitrification dominates anaerobic respiration. Overall, these findings suggest Mn cycling in continental slope sediments exposed to large riverine inputs may be more important than previously considered, and carbon remineralization via Mn reduction could contribute significantly to benthic DIC and alkalinity production.

Declaration of Competing Interest

None.

Acknowledgements

We would like to thank the captain and crew of the RV Savannah as well as Emily Buckley, Julien Richirt, and Andrew Stancil for help with sample collection and/or analysis. This research was supported by the National Science Foundation (OCE-1438648) to M. Taillefert, EC2CO-DRIL MissRhoDia project to C. Rabouille, National Academies of Science, Engineering, and Medicine Gulf Research Program (Early Career Grant 2000007281) to J. Beckler, and the Chateaubriand Fellowship of the Office for Science & Technology of the Embassy of France in the United States awarded to S. Owings. Finally, we thank the editor and

two anonymous reviewers for their insightful comments and suggestions which helped improve this paper significantly.

Appendix A. Supplementary data

Supplementary data to this article can be found online at https://doi.org/10.1016/j.marchem.2020.103908.

References

- Aller, R.C., 1982. Carbonate dissolution in Nearshore Terrigenous muds: the role of physical and biological reworking. J. Geol. 90 (1), 79–95.
- Aller, R.C., 1994. The sedimentary Mn cycle in Long Island sound: its role as intermediate oxidant and the influence of bioturbation, O₂, and Corg flux on diagenetic reaction balances. J. Mar. Res. 52 (2), 259–295.
- Aller, R.C., 1998. Mobile deltaic and continental shelf muds as suboxic, fluidized bed reactors. Mar. Chem. 61 (3), 143–155.
- Aller, R.C., Aller, J.Y., 1998. The effect of biogenic irrigation intensity and solute exchange on diagenetic reaction rates in marine sediments. J. Mar. Res. 56 (4), 905–936
- Aller, R.C., et al., 1990. Bioturbation and manganese cycling in hemipelagic sediments. Philos. Trans. R. Soc. Lond. Ser. A Math. Phys. Sci. 331 (1616), 51–68.
- Aller, R.C., Blair, N.E., Xia, Q., Rude, P.D., 1996. Remineralization rates, recycling, and storage of carbon in Amazon shelf sediments. Cont. Shelf Res. 16 (5), 753–786.
- Allison, M.A., Pratt, T.C., 2017. Discharge controls on the sediment and dissolved nutrient transport flux of the lowermost Mississippi River: implications for export to the ocean and for delta restoration. J. Hydrol. 555, 1–14.
- Allison, M.A., et al., 2012. A water and sediment budget for the lower Mississippi-Atchafalaya River in flood years 2008–2010: implications for sediment discharge to the oceans and coastal restoration in Louisiana. J. Hydrol. 432-433, 84-97.
- Andrews, D., Bennett, A., 1981. Measurements of diffusivity near the sediment-water interface with a fine-scale resistivity probe. Geochim. Cosmochim. Acta 45 (11), 2169–2175
- Anschutz, P., Sundby, B., Lefrancois, L., Luther, G.W., Mucci, A., 2000. Interactions between metal oxides and species of nitrogen and iodine in bioturbated marine sediments. Geochim. Cosmochim. Acta 64 (16), 2751–2763.
- Anschutz, P., Dedieu, K., Desmazes, F., Chaillou, G., 2005. Speciation, oxidation state, and reactivity of particulate manganese in marine sediments. Chem. Geol. 218 (3–4), 265–279
- Arnold, R.G., DiChristina, T.J., Hoffmann, M.R., 1988. Reductive dissolution of fe(III) oxides by Pseudomonas sp. 200. Biotechnol. Bioeng. 32 (9), 1081–1096.
- Beckler, J.S., Nuzzio, D.B., Taillefert, M., 2014. Development of single-step liquid chromatography methods with ultraviolet detection for the measurement of inorganic anions in marine waters. Limnol. Oceanogr. Methods 12 (8), 563–576.
- Beckler, J.S., Jones, M.E., Taillefert, M., 2015. The origin, composition, and reactivity of dissolved iron(III) complexes in coastal organic- and iron-rich sediments. Geochim. Cosmochim. Acta 152 (3), 72–88.
- Beckler, J.S., Kiriazis, N., Rabouille, C., Stewart, F.J., Taillefert, M., 2016. Importance of microbial iron reduction in deep sediments of river-dominated continental-margins. Mar. Chem. 178, 22–34.
- Bianchi, T.S., 2011. The role of terrestrially derived organic carbon in the coastal ocean: a changing paradigm and the priming effect. Proc. Natl. Acad. Sci. 108 (49), 19473.
- Bianchi, T.S., et al., 2006. Rapid export of organic matter to the Mississippi canyon. EOS Trans. Am. Geophys. Union 87 (50), 565–573.
- Bianchi, T.S., Galler, J.J., Allison, M.A., 2007. Hydrodynamic sorting and transport of terrestrially derived organic carbon in sediments of the Mississippi and Atchafalaya Rivers. Estuar. Coast. Shelf Sci. 73 (1), 211–222.
- Bianchi, T.S., et al., 2018. Centers of organic carbon burial and oxidation at the land-ocean interface. Org. Geochem. 115, 138–155.
- Blair, N.E., Aller, R.C., 2012. The fate of terrestrial organic carbon in the marine environment. Annu. Rev. Mar. Sci. 4 (1), 401–423.
- Boudreau, B.P., 1997. Diagenetic models and their implementation. Springer, Berlin. Bowles, M.W., Mogollón, J.M., Kasten, S., Zabel, M., Hinrichs, K.-U., 2014. Global rates of marine sulfate reduction and implications for sub-sea-floor metabolic activities. Science 344 (6186), 889.
- Brendel, P.J., Luther III, G.W., 1995. Development of a gold amalgam Voltammetric microelectrode for the determination of dissolved Fe, Mn, O2, and S(-II) in Porewaters of marine and freshwater sediments. Environ. Sci. Technol. 29 (3), 751–761
- Bristow, G., Taillefert, M., 2008. VOLTINT: a Matlab®-based program for semiautomated processing of geochemical data acquired by voltammetry. Comput. Geosci. 34 (2), 153–162.
- Cai, W.-J., Sayles, F.L., 1996. Oxygen penetration depths and fluxes in marine sediments. Mar. Chem. 52 (2), 123–131.
- Cai, W.-J., et al., 2011. Acidification of subsurface coastal waters enhanced by eutrophication. Nat. Geosci. 4, 766.
- Canfield, D.E., 1994. Factors influencing organic matter preservation in marine sediments. Chem. Geol. 114 (3–4), 315–329.
- Canfield, D.E., et al., 1993a. Pathways of organic carbon oxidation in three continental margin sediments. Mar. Geol. 113 (1), 27–40.

- Canfield, D.E., Thamdrup, B., Hansen, J.W., 1993b. The anaerobic degradation of organic matter in Danish coastal sediments: iron reduction, manganese reduction, and sulfate reduction. Geochim. Cosmochim. Acta 57 (16), 3867–3883.
- Clayton, T.D., Byrne, R.H., 1993. Spectrophotometric seawater pH measurements: total hydrogen ion concentration scale calibration of m-cresol purple and at-sea results. Deep-Sea Res. I Oceanogr. Res. Pap. 40 (10), 2115–2129.
- Corbett, D.R., McKee, B., Duncan, D., 2004. An evaluation of mobile mud dynamics in the Mississippi River deltaic region. Mar. Geol. 209 (1), 91–112.
- Corbett, D.R., McKee, B., Allison, M., 2006. Nature of decadal-scale sediment accumulation on the western shelf of the Mississippi River delta. Cont. Shelf Res. 26 (17), 2125–2140.
- Couture, R.-M., Shafei, B., Van Cappellen, P., Tessier, A., Gobeil, C., 2010. Non-steady state modeling of arsenic diagenesis in Lake sediments. Environ. Sci. Technol. 44 (1), 197–203.
- Cowie, G.L., Hedges, J.I., 1984. Carbohydrate sources in a coastal marine environment. Geochim. Cosmochim. Acta 48 (10), 2075–2087.
- Cowie, G.L., Hedges, J.I., 1992. Sources and reactivities of amino acids in a coastal marine environment. Geochim. Cosmochim. Acta 37 (4), 703–724.
- Davies, S.H.R., Morgan, J.J., 1989. Manganese(II) oxidation kinetics on metal oxide surfaces. J. Colloid Interface Sci. 129 (1), 63–77.
- Devereux, R., et al., 2015. Changes in northern Gulf of Mexico sediment bacterial and archaeal communities exposed to hypoxia. Geobiology 13 (5), 478–493.
- Devereux, R., et al., 2019. Spatially variable bioturbation and physical mixing drive the sedimentary biogeochemical seascape in the Louisiana continental shelf hypoxic zone. Biogeochemistry 143 (2), 151–169.
- Dickson, A.G., Sabine, C.L., Christian, J.R., 2007. Guide to best practices for ocean CO2 measurements. PICES Spec. Publ. 3.
- Dollhopf, M.E., Nealson, K.H., Simon, D.M., Luther, G.W., 2000. Kinetics of Fe(III) and Mn(IV) reduction by the Black Sea strain of Shewanella putrefaciens using in situ solid state voltammetric Au/Hg electrodes. Mar. Chem. 70 (1), 171–180.
- Duckworth, O.W., Martin, S.T., 2004. Role of molecular oxygen in the dissolution of siderite and rhodochrosite. Geochim. Cosmochim. Acta 68 (3), 607–621.
- Ellis, A.J., Golding, R.M., 1959. 25. Spectrophotometric determination of the acid dissociation constants of hydrogen sulphide. J. Chem. Soc. 127–130 (resumed)(0).
- Fennel, K., Testa, J.M., 2019. Biogeochemical controls on coastal hypoxia. Annu. Rev. Mar. Sci. 11 (1), 105–130.
- Ferdelman, T.G., Fossing, H., Neumann, K., Schulz, H.D., 1999. Sulfate reduction in surface sediments of the Southeast Atlantic continental margin between 15 degrees 38'S and 27 degrees 57'S (Angola and Namibia). Limnol. Oceanogr. 44 (3), 650–661.
- Froelich, P.N., et al., 1979. Early oxidation of organic matter in pelagic sediments of the eastern equatorial Atlantic: suboxic diagenesis. Geochim. Cosmochim. Acta 43 (7), 1075–1090.
- Geyer, W.R., Hill, P.S., Kineke, G.C., 2004. The transport, transformation and dispersal of sediment by buoyant coastal flows. Cont. Shelf Res. 24 (7), 927–949.
- Grasshoff, K., Kremling, K., Ehrhardt, M., 1999. Methods of Seawater Analysis. Wiley-VCH.
- Green, R.E., Bianchi, T.S., Dagg, M.J., Walker, N.D., Breed, G.A., 2006. An organic carbon budget for the Mississippi River turbidity plume and plume contributions to air-sea CO₂ fluxes and bottom water hypoxia. Estuar. Coasts 29 (4), 579–597.
- Grégoire, M., Friedrich, J., 2004. Nitrogen budget of the northwestern Black Sea shelf inferred from modeling studies and in situ benthic measurements. Mar. Ecol. Prog. Ser. 270, 15–39.
- Gustafsson, J.P., 2019. Visual MINTEQ, version 3.1. KTH Royal Institute of Technology, Stockholm, Sweden.
- Hall, P.J., Aller, R.C., 1992. Rapid, small-volume, flow injection analysis for SCO2, and NH4+ in marine and freshwaters. Limnol. Oceanogr. 37 (5), 1113–1119.
- Hartnett, H.E., Keil, R.G., Hedges, J.I., Devol, A.H., 1998. Influence of oxygen exposure time on organic carbon preservation in continental margin sediments. Nature 391 (6667), 572–575.
- Henneke, E., Luther, G.W., de Lange, G.J., 1991. Determination of inorganic Sulphur speciation with polarographic techniques: some preliminary results for recent hypersaline anoxic sediments. Mar. Geol. 100 (1), 115–123.
- Herszage, J., Dos Santos Afonso, M., 2003. Mechanism of hydrogen sulfide oxidation by manganese(IV) oxide in aqueous solutions. Langmuir 19, 9684–9692.
- Hu, X., Cai, W.-J., Wang, Y., Guo, X., Luo, S., 2011. Geochemical environments of continental shelf-upper slope sediments in the northern Gulf of Mexico. Palaeogeogr. Palaeoclimatol. Palaeoecol. 312 (3), 265–277.
- Hyacinthe, C., Van Cappellen, P., 2004. An authigenic iron phosphate phase in estuarine sediments: composition, formation and chemical reactivity. Mar. Chem. 91, 227–251.
- Hyacinthe, C., Anschutz, P., Carbonel, P., Jouanneau, J.M., Jorissen, F.J., 2001. Early diagenetic processes in the muddy sediments of the Bay of Biscay. Mar. Geol. 177 (1), 111–128.
- Hyun, J.H., et al., 2017. Manganese and iron reduction dominate organic carbon oxidation in surface sediments of the deep Ulleung Basin, East Sea. Biogeosciences 14 (4), 941–958.
- Jilbert, T., Slomp, C.P., 2013. Iron and manganese shuttles control the formation of authigenic phosphorus minerals in the euxinic basins of the Baltic Sea. Geochimica et Cosmochimica Acta 107, 155–169.
- Jones, M., Fennessey, C.M., DiChristina, T.J., Taillefert, M., 2010. Shewanella oneidensis MR-1 mutants selected for their inability to produce soluble organic-Fe(III) complexes are unable to respire Fe(III) as anaerobic electron acceptor. Environ. Microbiol. 12 (4), 938–950.
- Jørgensen, B.B., 1982. Mineralization of organic matter in the sea bed—the role of sulphate reduction. Nature 296 (5858), 643–645.

Kostka, J.E., Luther, G.W., 1994. Partitioning and speciation of solid phase iron in saltmarsh sediments. Geochim. Cosmochim. Acta 58 (7), 1701–1710.

- Lan, S., et al., 2017. Mechanisms of Mn(II) catalytic oxidation on ferrihydrite surfaces and the formation of manganese (oxyhydr)oxides. Geochim. Cosmochim. Acta 211, 79-96.
- Larsen, I., et al., 1998. Manganite reduction by Shewanella putrefaciens MR-4. Am. Mineral. 83 (11-12 Part 2), 1564–1572.
- Law, G.T.W., et al., 2009. Manganese, iron, and Sulphur cycling on the Pakistan margin. Deep-Sea Res. II Top. Stud. Oceanogr. 56 (6), 305–323.
- Lee, T., Hyun, J.H., Mok, J.S., Kim, D., 2008. Organic carbon accumulation and sulfate reduction rates in slope and basin sediments of the Ulleung Basin, east/Japan Sea. Geo-Mar. Lett. 28 (3), 153–159.
- Lehrter, J.C., Beddick Jr., D.L., Devereux, R., Yates, D.F., Murrell, M.C., 2012. Sediment-water fluxes of dissolved inorganic carbon, O₂, nutrients, and N₂ from the hypoxic region of the Louisiana continental shelf. Biogeochemistry 109 (1–3), 233–252.
- Lenstra, W.K., et al., 2019. The shelf-to-basin iron shuttle in the Black Sea revisited. Chem. Geol. 511, 314–341.
- Lenstra, W.K., Séguret, M.J.M., Behrends, T., Groeneveld, R.K., Hermans, M., Witbaard, R., Slomp, C.P., 2020. Controls on the shuttling of manganese over the northwestern Black Sea shelf and its fate in the euxinic deep basin. Geochim. Cosmochim. Acta 273, 177–204.
- Lin, S., Morse, J.W., 1991. Sulfate reduction and iron sulfide mineral formation in Gulf of Mexico anoxic sediments. Am. J. Sci. 291 (1), 55–89.
- Lin, S., Huang, K.-M., Chen, S.-K., 2002. Sulfate reduction and iron sulfide mineral formation in the southern East China Sea continental slope sediment. Deep-Sea Res. I Oceanogr. Res. Pap. 49 (10), 1837–1852.
- Lovley, D.R., Phillips, E.J.P., 1988. Novel mode of microbial energy metabolism: organic carbon oxidation coupled to Dissimilatory reduction of Iron or manganese. Appl. Environ. Microbiol. 54 (6), 1472–1480.
- Luther, G.W., et al., 2008. Use of voltammetric solid-state (micro)electrodes for studying biogeochemical processes: laboratory measurements to real time measurements with an in situ electrochemical analyzer (ISEA). Mar. Chem. 108 (3), 221–235.
- Lyons, K., Severmann, C.K., 2006. A critical look at iron paleoredox proxies: New insights from modern euxinic marine basins. Geochimica et Cosmochimica Acta 70, 5698–5722.
- Madison, A.S., Tebo, B.M., Luther, G.W., 2011. Simultaneous determination of soluble manganese(III), manganese(II) and total manganese in natural (pore)waters. Talanta 84 (2), 374–381.
- McCarthy, M.J., Newell, S.E., Carini, S.A., Gardner, W.S., 2015. Denitrification dominates sediment nitrogen removal and is enhanced by bottom-water hypoxia in the northern Gulf of Mexico. Estuar. Coasts 38 (6), 2279–2294.
- McKee, B.A., Aller, R.C., Allison, M.A., Bianchi, T.S., Kineke, G.C., 2004. Transport and transformation of dissolved and particulate materials on continental margins influenced by major rivers: benthic boundary layer and seabed processes. Cont. Shelf Res. 24 (7), 899–926.
- Meiggs, D., Taillefert, M., 2011. The effect of riverine discharge on biogeochemical processes in estuarine sediments. Limnol. Oceanogr. 56 (5), 1797–1810.
- Millero, F.J., Sotolongo, S., Izaguirre, M., 1987. The oxidation kinetics of Fe(II) in seawater. Geochim. Cosmochim. Acta 51 (4), 793–801.
- Milliman, J.D., Meade, R.H., 1983. World-wide delivery of river sediment to the Oceans. J. Geol. 91 (1). 1–21.
- Morse, J.W., Beazley, M.J., 2008. Organic matter in deepwater sediments of the Northern Gulf of Mexico and its relationship to the distribution of benthic organisms. Deep Sea Res. II 55, 2563–2571.
- Morse, J.W., Rowe, G.T., 1999. Benthic biogeochemistry beneath the Mississippi River plume. Estuaries 22 (2), 206–214.
- Mossa, J., 1996. Sediment dynamics in the lowermost Mississippi River. Eng. Geol. 45 (1), 457–479.
- Mouret, A., et al., 2009. Benthic geochemistry of manganese in the Bay of Biscay, and sediment mass accumulation rate. Geo-Mar. Lett. 29 (3), 133–149.
- Murphy, J., Riley, J.P., 1962. A modified single solution method for the determination of phosphate in natural waters. Anal. Chim. Acta 27, 31–36.
- Myers, C.R., Nealson, K.H., 1988. Bacterial manganese reduction and growth with manganese oxide as the sole Electron acceptor. Science 240 (4857), 1319–1321.
- Oldham, V.E., et al., 2019. The speciation and mobility of Mn and Fe in estuarine sediments. Aquat. Geochem. 25 (1), 3–26.
- Owings, S., Luther III, G.W., Taillefert, M., 2019. Development of a rate law for arsenite oxidation by manganese oxides. Geochimica et Cosmochimica Acta 250, 251–267.
- Pyzik, A.J., Sommer, S.E., 1981. Sedimentary iron monosulfides: kinetics and mechanism of formation. Geochim. Cosmochim. Acta 45 (5), 687–698.
- Rabalais, N.N., Turner, R.E., 2017. Summary of 2017 Research Cruise Press Release (Gulf of Mexico).
- Rabalais, N.N., et al., 2007. Hypoxia in the northern Gulf of Mexico: does the science support the plan to reduce, mitigate, and control hypoxia? Estuar. Coasts 30 (5), 753–772.
- Raiswell, R., Vu, H.P., Brinza, L., Benning, L.G., 2010. The determination of labile Fe in ferrihydrite by ascorbic acid extraction: methodology, dissolution kinetics and loss of solubility with age and de-watering. Chem. Geol. 278, 70–79.
- Rassmann, J., Lansard, B., Pozzato, L., Rabouille, C., 2016. Carbonate chemistry in sediment porewaters of the Rhône River delta driven by early diagenesis (northwestern Mediterranean). Biogeosciences 13 (18), 5379–5394.
- Reiman, J.H., Xu, Y.J., He, S., DelDuco, E.M., 2018. Metals geochemistry and mass export from the Mississippi-Atchafalaya River system to the Northern Gulf of Mexico. Chemosphere 205, 559–569.
- Revsbech, N.P., 1989. An oxygen microsensor with a guard cathode. Limnol. Oceanogr. 34 (2), 474–478.

S.M. Owings et al.

- Richard, D., Sundby, B., Mucci, A., 2013. Kinetics of manganese adsorption, desorption, and oxidation in coastal marine sediments. Limnol. Oceanogr. 58 (3), 987–996.
- Rickard, D., Luther, G.W., 1997. Kinetics of pyrite formation by the H2S oxidation of iron (II) monosulfide in aqueous solutions between 25 and 125 degrees C: the mechanism. Geochim. Cosmochim. Acta 61 (1), 135–147.
- Rowe, G.T., Kaegi, M.E.C., Morse, J.W., Boland, G.S., Escobar Briones, E.G., 2002. Sediment community metabolism associated with continental shelf hypoxia, Northern Gulf of Mexico. Estuaries 25 (6), 1097–1106.
- Rowe, G.T., Morse, J., Nunnally, C., Boland, G.S., 2008. Sediment community oxygen consumption in the deep Gulf of Mexico. Deep-Sea Res. II Top. Stud. Oceanogr. 55 (24), 2686–2691.
- Sampere, T.P., Bianchi, T.S., Allison, M.A., McKee, B.A., 2011. Burial and degradation of organic carbon in Louisiana shelf/slope sediments. Estuar. Coast. Shelf Sci. 95 (1), 232, 244
- Scholz, F., et al., 2011. Early diagenesis of redox-sensitive trace metals in the Peru upwelling area response to ENSO-related oxygen fluctuations in the water column. Geochimica et Cosmochimica Acta 75, 7257–7276.
- Scholz, F., McManus, J., Sommer, S., 2013. The manganese and iron shuttle in a modern euxinic basin and implications for molybdenum cycling at euxinic ocean margins. Chem. Geol. 355, 56–68.
- Scholz, F., et al., 2019. Shelf-to-basin iron shuttle in the Guaymas Basin, Gulf of California. Geochimica et Cosmochimica Acta 261, 76–92.
- Soetaert, K., Herman, P.M.J., Middelburg, J.J., 1996. A model of early diagenetic processes from the shelf to abyssal depths. Geochim. Cosmochim. Acta 60 (6), 1019–1040
- Sørensen, J., Jeørgensen, B.B., 1987. Early diagenesis in sediments from Danish coastal waters: microbial activity and Mn-Fe-S geochemistry. Geochim. Cosmochim. Acta 51 (6), 1583–1590.
- Stookey, L.L., 1970. Ferrozine- a new spectrophotometric reagent for Iron. Anal. Chem. 42 (7), 779-781.
- Strickland, J.D.H., Parsons, T.R., 1972. A Practical Handbook of Sea-Water Analysis. Stumm, W., Morgan, J.J., 1996. Aquatic Chemistry: Chemical Equilibria and Rates in Natural Waters. John Wiley & Sons, Inc., New York, New York.
- Sundby, B., Silverberg, N., 1985. Manganese fluxes in the benthic boundary layer1. Limnol. Oceanogr. 30 (2), 372–381.
- Sundby, B., Silverberg, N., Chesselet, R., 1981. Pathways of manganese in an open estuarine system. Geochim. Cosmochim. Acta 45 (3), 293–307.
- Sutula, M., Bianchi, T.S., McKee, B.A., 2004. Effect of seasonal sediment storage in the lower Mississippi River on the flux of reactive particulate phosphorus to the Gulf of Mexico, Limnol. Oceanogr. 49 (6), 2223–2235.
- Taillefert, M., Bono, A.B., Luther, G.W., 2000. Reactivity of freshly formed Fe(III) in synthetic solutions and (pore)waters: voltammetric evidence of an aging process. Environ. Sci. Technol. 34 (11), 2169–2177.

- Taillefert, M., et al., 2007. Shewanella putrefaciens produces an Fe(III)-solubilizing ligand during anaerobic respiration on insoluble Fe(III) oxides. J. Inorg. Biochem. 101 (11), 1760–1767.
- Taillefert, M., et al., 2017. Early diagenesis in the sediments of the Congo deep-sea fan dominated by massive terrigenous deposits: part II Iron–sulfur coupling. Deep-Sea Res. II Top. Stud. Oceanogr. 142, 151–166.
- Tessier, A., Campbell, P.G.C., Bisson, M., 1979. Sequential extraction procedure for the speciation of particulate trace metals. Anal. Chem. 51 (7), 844–851.
- Thamdrup, B., Rosselló-Mora, R., Amann, R., 2000. Microbial manganese and sulfate reduction in Black Sea shelf sediments. Appl. Environ. Microbiol. 66 (7), 2888–2897.
- Theberge, S.M., Luther, G.W., 1997. Determination of the electrochemical properties of a soluble aqueous FeS species present in Sulfidic solutions. Aquat. Geochem. 3 (3), 191–211
- Trefry, J.H., Presley, B.J., 1982. Manganese fluxes from Mississippi Delta sediments. Geochim. Cosmochim. Acta 46 (10), 1715–1726.
- Turner, R.E., Rabalais, N.N., Alexander, R.B., McIsaac, G., Howarth, R.W., 2007.
 Characterization of nutrient, organic carbon, and sediment loads and concentrations from the Mississippi River into the northern Gulf of Mexico. Estuar. Coasts 30 (5), 773–790
- Viollier, E., Inglett, P.W., Hunter, K., Roychoudhury, A.N., Van Cappellen, P., 2000. The ferrozine method revisited: Fe(II)/Fe(III) determination in natural waters. Appl. Geochem. 15 (6), 785–790.
- Wade, T.L., Soliman, Y., Sweet, S.T., Wolff, G.A., Presley, B.J., 2008. Trace elements and polycyclic aromatic hydrocarbons (PAHs) concentrations in deep Gulf of Mexico sediments. Deep-Sea Res. II Top. Stud. Oceanogr. 55 (24), 2585–2593.
- Wang, Y., Van Cappellen, P., 1996. A multicomponent reactive transport model of early diagenesis: application to redox cycling in coastal marine sediments. Geochim. Cosmochim. Acta 60 (16), 2993–3014.
- Waterson, E.J., Canuel, E.A., 2008. Sources of sedimentary organic matter in the Mississippi River and adjacent Gulf of Mexico as revealed by lipid biomarker and δ13CTOC analyses. Org. Geochem. 39 (4), 422–439.
- Xu, K., Harris, C.K., Hetland, R.D., Kaihatu, J.M., 2011. Dispersal of Mississippi and Atchafalaya sediment on the Texas–Louisianashelf: Model estimates for the year 1993. Cont. Shelf Res.Sci. 31, 1558–1575.
- Xu, K., et al., 2014. Seabed erodibility variations on the Louisiana continental shelf before and after the 2011 Mississippi River flood. Estuar. Coast. Shelf Sci. 149, 283–293
- Yeager, K.M., Santschi, P.H., Rowe, G.T., 2004. Sediment accumulation and radionuclide inventories (239,240Pu, 210Pb and 234Th) in the northern Gulf of Mexico, as influenced by organic matter and macrofaunal density. Mar. Chem. 91 (1), 1–14.
- Zhuang, G.-C., Montgomery, A., Joye, S.B., 2019. Heterotrophic metabolism of C1 and C2 low molecular weight compounds in northern Gulf of Mexico sediments: controlling factors and implications for organic carbon degradation. Geochim. Cosmochim. Acta 247, 243–260.